A direct numerical simulation study of turbulence and flame structure in transverse jets analysed in jet-trajectory based coordinates

R. W. Grout[1]†, **A. Gruber**[2], **H. Kolla**[3], **P.-T. Bremer**[4], **J. C. Bennett**[3], **A. Gyulassy**[5] **and J. H. Chen**[3]

[1] National Renewable Energy Laboratory, Golden, CO 80401, USA
[2] SINTEF Energy Research, 7465 Trondheim, Norway
[3] Sandia National Laboratories, Livermore, CA 94550, USA
[4] Lawrence Livermore National Laboratories, Livermore, CA 94551, USA
[5] University of Utah, Salt Lake City, UT 84112, USA

An H_2/N_2 jet in cross-flow (JICF) of air is studied using three-dimensional direct numerical simulation with and without chemical reaction in order to investigate the role of the complex JICF turbulent flow field in the mechanism of fast fuel-oxidant mixing and of aerodynamic flame stabilization in the near field of the jet nozzle. Focus is on delineating the flow/mixing/chemistry conditions that are necessary and/or sufficient to achieve flame anchoring that ultimately enables the formulation of more reliable and precise guidelines for design of fuel injection nozzles. A mixture averaged diffusion formulation that includes the effect of thermal diffusion is used along with a detailed chemical kinetics mechanism for hydrogen–air combustion. A new parametrization technique is used to describe the jet trajectory: solution of Laplace's equation upon, and then within, an opportune scalar surface anchored by Dirichlet boundary conditions at the jet nozzle and plume exit from the domain provides a smoothly varying field along the jet path. The surface is selected to describe the scalar mixing and reaction associated with a transverse jet. The derived field, $j(\boldsymbol{x})$, is used as a condition to mark the position along the natural jet trajectory when analysing the variation of relevant flow, mixing and reaction quantities in the present direct numerical simulation (DNS) datasets. Results indicate the presence of a correlation between the flame base location in parameter space and a region of low velocity magnitude, high enstrophy, high mixing rate and high equivalence ratio (flame root region). Instantaneously, a variety of vortical structures, well known from the literature as important contributors to fuel-oxidant mixing, are observed in both inert and reactive cases with a considerable span in length scales. Moreover, instantaneous plots from reactive cases illustrate that the most upstream flame tongues propagate close to the trailing edge of the fuel jet potential core near the jet shear layer vortex shedding position. Some degree of asymmetry with respect to the domain mid-plane in the spanwise direction is observed in the averaged fields, both for the inert and reactive cases.

Key words: jets, turbulent mixing, turbulent reacting flows

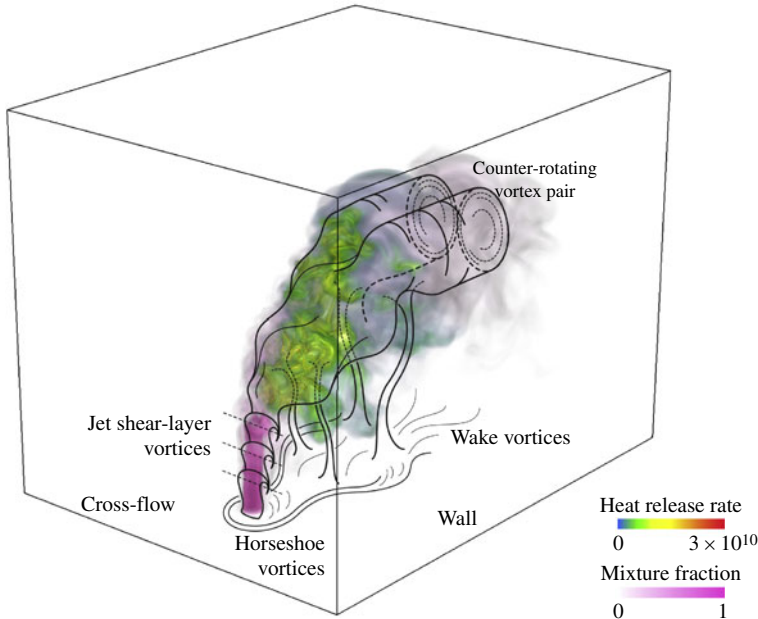† Email address for correspondence: ray.grout@cantab.net

FIGURE 1. Volume rendering of heat-release rate and mixture fraction fields for reacting jet
in cross-flow, annotated to illustrate key vortical structures.

1. Introduction

Transverse jets, or jets in cross-flow (JICF), result from the combination of two
canonical flows: a boundary layer flow and a jet flow issuing from a nozzle in
quiescent fluid. The interaction of these two simple flows results in a complex,
unsteady, fully three-dimensional flow field. Bagheri *et al.* (2009) recently showed
that the characteristic self-sustained instabilities are responsible for the formation of
a number of vortical structures characteristic of the JICF configuration. A large body
of literature, mostly on non-reacting transverse jet configurations, has accumulated
over the years, and a recent comprehensive review is given in Karagozian (2010).
Experimental investigations describing the complex vortical structures of the JICF
flow field are numerous: for example, Andreopoulos & Rodi (1984), Andreopoulos
(1985), Coelho & Hunt (1989), Fric & Roshko (1994), Kelso, Lim & Perry (1996),
Haven & Kurosaka (1997), Cortelezzi & Karagozian (2001) and Gutmark, Ibrahim &
Murugappan (2008). Typically, four distinct types of vortical structures are observed in
JICF configurations: (i) the counter-rotating vortex pair (CVP) formed just downstream
of the jet and elongated in the cross-flow direction; (ii) the vortices formed in the
shear layer (SLVs) between the jet and the cross-flow; (iii) the horseshoe or necklace
vortex (HSV) formed close to the wall both upstream and downstream of the jet
nozzle; and (iv) the wake vortices (WVs), whose structure is elongated in the wall-
normal direction, generated in the jet near field and then convected downstream by
the cross-flow motion. These structures are illustrated in figure 1. The role of the
HSV in the formation of the complex flow field of the transverse jet configuration
has been discussed extensively in the literature (see citations above and below), but
observations based on the present datasets and on previous work (Grout *et al.* 2011)

seem to indicate a limited direct relevance of the HSV on fuel-oxidant mixing and flame anchoring.

The combination of large-scale flow structures furnishing efficient entrainment and intense, small-scale vorticity delivers rapid mixing. JICF configurations are often employed in practical applications where this fast mixing is desired; typical examples are gas turbine blade film cooling (Jessen, Schröder & Klaas 2007) and fuel injection into the premixer section of a gas turbine burner that operates in a lean premixed (LPM) combustion mode (Döbbeling, Hellat & Koch 2007). This work focuses on the latter.

Despite the importance of this configuration in reactive flows, much of the attention in previous work has focused on large-scale flow structure development, jet trajectories, scalar-mixing and transport properties, and other associated flow phenomena, in non-reacting flows. Holdeman (1972), Fearn & Weston (1974, 1975, 1978, 1979) conducted seminal experimental studies aimed at the formulation of empirical formulas to determine the jet trajectory and its penetration into the cross-flow and at a first description of the JICF pressure field. More recent efforts have tried to improve the JICF scaling laws and adopted analytical approaches through similarity analysis in order to characterize the main features of the transverse jet configurations from the near to the far field (Broadwell & Breidenthal 1984; Smith & Mungal 1998; Hasselbrink & Mungal 2001*a*; Muppidi & Mahesh 2005). The importance of the jet velocity profile and the nozzle shape on the resulting JICF flow field is discussed in recent experimental and modelling studies (Muppidi & Mahesh 2005; New, Lim & Luo 2006; Salewski, Stankovic & Fuchs 2008), and the scalar mixing field in transverse jets is studied by Su & Mungal (2004) and Muppidi & Mahesh (2008). A relatively limited body of experimental and analytical studies is available considering reactive JICF configurations. Early experimental studies focused on radiation from large flares (Brzustowski, Gollahalli & Sullivan 1975; Schmitt 1985). More recently Gollahalli & Pardiwalla (2002) have addressed the problem of flame stability for JICF configurations, and Hasselbrink & Mungal (2001*b*) present a characterization of the JICF flow field in the presence of a flame.

The present work is an investigation into the physical mechanism of flame stabilization downstream of a transverse fuel jet in oxidant cross-flow and its relation to the turbulent scalar mixing field. A direct numerical simulation (DNS) is conducted of a hydrogen–air flame anchored above a round jet nozzle. Grout *et al.* (2011) simulated a similar configuration with a square nozzle and observed qualitatively that the flame appeared to be stabilized with the aid of shear layer vortices, in a region where the mixture is near-stoichiometric and the flow has relatively low velocity. Here, we apply comprehensive analytics to quantify the flow–chemistry interaction in the JICF *natural* frame of reference. To this end, *chemical explosive mode analysis* (see § 3.1) is used to analyse the chemical processes, and the spatial coordinates are mapped to a new jet path parametrization described in § 3.2, which is based on the solution of Laplace's equation on an opportunely chosen scalar surface describing the jet.

The remainder of this paper is organized as follows. The governing equations and the problem formulation are presented in § 2.1, followed by a brief discussion of the numerical methods in the DNS code, S3D, used to perform the present simulations in §§ 2.2 and 2.3. The key analytical techniques are discussed in the following sections: chemical explosive mode analysis (CEMA) is reviewed in § 3.1 and the new jet path parametrization is introduced in § 3.2. Instantaneous and time-averaged results from the reacting DNS are presented in § 4; results from DNS of an analogous inert case are

also used to facilitate the discussion of the reacting results. Finally, conclusions and recommendations for further work are presented in § 5.

2. Formulation

2.1. *Mathematical description and configuration*

The Navier–Stokes equations in their compressible formulation are solved in a three-dimensional computational domain to simulate: (i) the interaction of a non-reactive transverse H_2/N_2 fuel jet with a cross-flow of air; (ii) the combustion behaviour of the hydrogen–air flame aerodynamically stabilized in the near field of the transverse jet immediately downstream of the fuel nozzle. The homogeneous chemical reactions in the gaseous phase are described by a detailed chemical kinetics mechanism for hydrogen combustion in air (Li *et al.* 2004). The mechanism contains nine species and 19 elementary reaction steps. Nitrogen is assumed inert in this context; NO_x-formation reactions are not included. Thermodynamic properties are modelled as polynomial functions of temperature and transport coefficients, as described in the CHEMKIN and TRANSPORT packages, respectively (Kee *et al.* 1999). Radiative heat transfer is assumed to be negligible, and is therefore not incorporated into the present simulation.

The jet fluid consists of 70 % hydrogen and 30 % nitrogen (by volume) and issues into the cross-flow of air from a round, 1 mm diameter hole flush with a smooth solid surface. The jet Reynolds number is $Re_j = u_j d/\nu \sim 4000$, where u_j is the jet bulk velocity, d is the nozzle diameter and ν is the kinematic viscosity of the jet fluid. The velocity and momentum flux ratios for the present configuration are $R_v = 4.5$ and $R_m = 3.4$, respectively. A symmetric, top-hat-shaped profile is assigned to the jet wall-normal velocity component while the other two components are set to zero. New *et al.* (2006) experimentally compared the behaviour of top-hat and parabolic JICF arrangements at similar momentum ratios, and found that while the time-averaged flows exhibit many similar features, the thinner shear layer in the top-hat profile led to earlier onset of more coherent leading-edge and lee-side vortices. From the perspective of attempting to generate a database for model development, an additional benefit to using a top-hat profile, such as the one that arises from nozzle flow, is that the jet boundary condition can be unambiguously specified and the results are not dependent on assumptions about the nature of – or interactions with – a notional pipe upstream of the jet inlet, such as would be the case for a parabolic profile. Turbulent velocity fluctuations are not imposed on the jet due to its relatively low Reynolds number. The latter boundary condition specification relies on the assumption that jet velocity fluctuations in themselves ultimately play a minor role in the transverse jet's behaviour compared to the approaching cross-flow turbulence, the turbulence generated by the interaction of the jet with the cross-flow and the jet wall-normal velocity mean profile itself (New *et al.* 2006).

The cross-flow of air enters the domain from a non-reflecting inflow boundary. The velocity fluctuations imposed at the domain's cross-flow inlet are obtained by temporal sampling time-evolving turbulence at a fixed streamwise location in an auxiliary DNS of a non-reactive turbulent boundary layer over a flat plate. This approach, which permits eddies to 'evolve' on the boundary, provides a more realistic description of the incoming turbulence compared with the usual practice of convecting a turbulence field at one time instant into the domain by Taylor's hypothesis. The simulation used to generate the inflow data is described in detail in § 2.3.

The three-dimensional Cartesian grid is uniform in the streamwise and spanwise directions and is refined in the wall-normal direction near the solid surface using a

tanh mapping. The first point off the wall is at $y^+ = 0.5$, where the superscript $+$ indicates non-dimensionalization by the viscous length scale. There are two points within $y^+ = 1$ and 13 points within $y^+ = 10$ to satisfy the resolution requirements in the viscous layer (Moser, Kim & Mansour 1999). Navier–Stokes characteristic boundary conditions (NSCBC) are implemented based on Poinsot & Lele (1992) and Sutherland & Kennedy (2003). The boundary conditions for the transverse jet cases are non-reflecting at the inflow ($x = 0$) and outflow ($x = L_x$, $y = L_y$) planes and no-slip isothermal, solid surface at the wall boundary ($y = 0$). The wall is assumed to be impermeable, so the wall-normal mass flux of all chemical species is set to zero. In the spanwise directions, the walls are located by design to be sufficiently far from the jet that they do not interact with the plume or flame, and are specified as periodic for consistency with the inflow boundary layer solution. Some important parameters are summarized in table 1. The simulations were performed at atmospheric pressure; the temperature of the wall and of the cross-flow air is 750 K, and that of the H_2/N_2 jet is 420 K. These temperatures are within the nominal temperature range of the fuel stream and of the combustion air delivered by the compression stage in large, stationary gas turbines for power generation in the 200–400 MW range.

The reacting JICF case (REJICF) was initialized by transitioning from a previous square jet reacting solution (Grout *et al.* 2011) to a round jet. The previous square jet solution was initialized by using a relatively coarse mesh, comparable to non-reacting JICF (NRJICF), to establish the jet plume, which was then ignited by imposing an 'ignition source' – fixing the temperature and composition at the adiabatic burned state in a small, cylindrical region (0.25 mm diameter, extending across the spanwise direction) of the domain on the leeward side of the jet – for a brief time, 8 μs. The solution was then up-sampled to the production grid resolution; before collecting data in the previous square jet study, all of the fluid present in the domain when the ignition source was removed was allowed to exit through the outflow boundary. At the end of the square jet data collection period reported in Grout *et al.* (2011), the jet nozzle was changed to a round profile; the transition was completed at $t/t_f = -0.5845$, where t_f is the domain flow-through (residence) time based on the mean cross-flow velocity, and the fuel in the jet was allowed to exit the domain (taking slightly less than t_f due to the added momentum from the jet and heat release from the flame) before data collection for this study commenced.

2.2. *The DNS code*

The parallel DNS code, S3D, developed at the Combustion Research Facility at Sandia National Laboratories by Chen *et al.* (2009), is used to perform the present simulations. In addition to the previous JICF study (Grout *et al.* 2011), S3D has been used for a range of studies, including premixed flames (Hawkes & Chen 2005; Sankaran *et al.* 2007; Gruber *et al.* 2010), non-premixed flames, (Hawkes *et al.* 2007; Yoo, Sankaran & Chen 2009), and auto-ignition (Echekki & Chen 2003; Sankaran *et al.* 2005).

S3D is written in FORTRAN 90 and uses the message passing interface (MPI) for interprocess communication in parallel execution. The algorithm implemented in S3D solves the Navier–Stokes equations for a compressible fluid in conservative form on a structured, Cartesian mesh in one, two or three spatial directions. Spatial derivatives are computed with an eighth-order, explicit, centred, finite-difference scheme (third-order one-sided stencils are used at the domain boundaries in the non-homogeneous directions) in conjunction with a tenth-order, explicit, spatial filter, as described in Kennedy & Carpenter (1994), to remove high-frequency noise and reduce aliasing

Case name	$L_x \times L_y \times L_z$	$N_x \times N_y \times N_z$	Cross-flow transit time (ms)	$x = 0/L_x$	$y = 0/L_y$	$z = 0/L_z$
TBLAUX	$40d \times 20d \times 20d$	$384 \times 240 \times 300$	0.714	periodic	INSW/NRO	periodic
NRJICF	$20d \times 20d \times 20d$	$300 \times 240 \times 300$	0.357	NRI/NRO	INSW/NRO	NRO/NRO
REJICF	$25d \times 20d \times 20d$	$1408 \times 1080 \times 1100$	0.446	NRI/NRO	INSW/NRO	periodic

TABLE 1. DNS parameters for the auxiliary turbulent boundary layer and production transverse jets: d is the jet diameter, $L_{(xyz)}$, $N_{(xyz)}$ the domain length and grid size in the x- y- and z-directions, respectively. NRI, non-reflecting inlet; NRO, non-reflecting outlet; INSW, inert no-slip wall.

errors. A fourth-order, six-stage, explicit Runge–Kutta scheme, described in Kennedy, Carpenter & Lewis (2000), is used for time integration.

2.3. *Auxiliary DNS and inflow boundary layer*

A turbulent boundary layer auxiliary DNS (TBLAUX) is performed for a non-reacting, periodic boundary layer flow to provide the transverse jet cases with an initial turbulence field and inlet turbulence. It is also used to validate the present code against well-known, incompressible, flat-plate boundary layer data from Wu & Moin (2009) and Jiménez *et al.* (2010). The auxiliary DNS is performed in a domain with dimensions $4\delta_{99\%}^f \times 2\delta_{99\%}^f \times \delta_{99\%}^f$, where $\delta_{99\%}$ indicates the boundary layer thickness defined as the height at which the streamwise velocity reaches 99 % of the free-stream velocity, to encompass the turbulent boundary layer structures (Tomkins & Adrian 2003). This simulation is initialized by superimposing compressible isotropic turbulence from a model spectrum (Passot & Pouquet 1987) onto an assumed-average-streamwise-velocity profile with an initial boundary layer thickness of $\delta_{99\%}^0 \sim 7$ mm. After an initial transient of 4 domain transit times, it is assumed that a realistic boundary layer turbulence is developed. The velocity field is then sampled on a y–z-plane at a fixed streamwise location for 5 additional domain transit times.

The boundary layer thickness of the approaching cross-flow evolves from $\delta_{99\%}^i \sim 11$ mm to $\delta_{99\%}^f \sim 12$ mm at the jet nozzle location during a typical non-reactive, transverse jet production run where the superscripts i and f indicate the initial and the final value of the boundary layer thickness, respectively. This corresponds to a Reynolds number $Re_{\delta_{99\%}}$ in the range of 8200–8900 based on the free-stream average velocity, $U_{cf} \sim 56.5$ m s^{-1}, on the boundary layer thickness $\delta_{99\%}$, and on the kinematic viscosity of air. The average viscous length scale is $\delta_\nu \sim 29.9$ µm, and the average friction velocity is $u_\tau \sim 2.52$ m s^{-1}. Both of these quantities are estimated from the local streamwise velocity gradient at the wall.

The procedure used here for the auxiliary DNS through a simple periodic boundary condition in the streamwise direction recycles the velocity field at the domain outlet and introduces it unchanged at the domain inlet without rescaling it, as is done by Spalart (1988) and more recently by Lund, Squires & Wu (2003). The present choice has the following trade-off: on one hand, the boundary layer grows slowly throughout the simulation, resulting in a slight non-stationarity; on the other hand, the entry length problems described in Simens *et al.* (2009) that arise from rescaling the velocity field are avoided, thereby permitting a shorter domain size in the streamwise direction. The primary objective of the present study is the investigation of the interaction between the cross-flow and the transverse jets and not the flat-plate boundary layer turbulence; therefore, to minimize the cost of the auxiliary simulation, it is assumed that any change in the cross-flow boundary layer thickness experienced by the transverse jets in the relatively short production runs is insignificant. Results from the auxiliary DNS are shown in figure 2, where the normalized mean velocity profile is plotted against the wall distance at the beginning ($t = 3$ ms), and end ($t = 7$ ms), of the velocity field sampling period. As is evident from the figure, the increase of the boundary layer thickness is minimal.

Figure 3 presents a comparison of the normalized streamwise velocity profile from the present auxiliary DNS dataset with other direct simulations of incompressible flat-plate turbulent boundary layers (Wu & Moin 2009) and shows very good agreement up to $y^+ \sim 200$ for $Re_\theta = 800$ and $Re_\theta = 900$ from Wu & Moin (2009) (open symbols ∇ and $\square$, respectively), where Re_θ is the Reynolds number based on the boundary
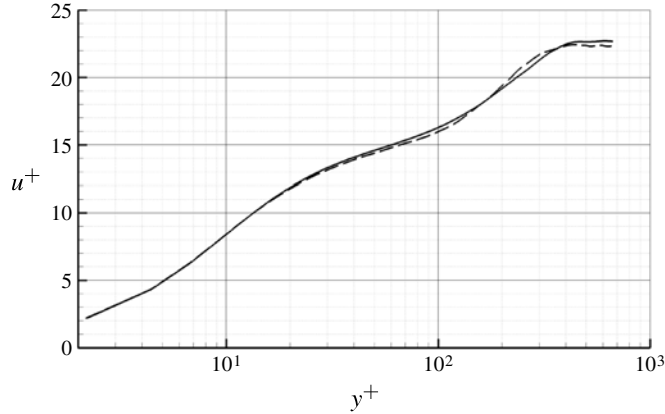
FIGURE 2. Normalized mean velocity profiles from the present auxiliary DNS at $t = 3$ ms (dashed line) and at $t = 7$ ms (solid line).
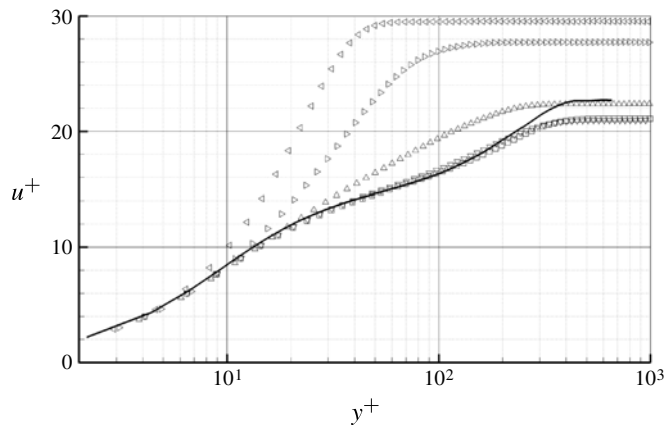

FIGURE 3. Comparison with other well-known datasets from the open literature. Solid line, present dataset; open symbols, transitional flat-plate boundary layer from Wu & Moin (2009).

layer momentum thickness. Some disagreement is expected for larger wall distances due to the compressible formulation used here that ultimately heats up the flow and due to the relatively small distance between $\delta_{99\%}$ and the domain upper boundary, y_L. Moreover, differences are expected outside the viscous sublayer between the present DNS and the transitional boundary layers for $Re_\theta = 200$, $Re_\theta = 400$ and $Re_\theta = 600$ (open symbols $\triangleleft$, $\triangleright$ and $\triangle$, respectively).

3. Analysis techniques

3.1. *Chemical explosive mode analysis*

Exploring the turbulence structures in the vicinity of the flame stabilization requires a quantitative definition that is used to demarcate the regions where the thermochemical state favours stabilization. Lu *et al.* (2010) proposed the CEMA procedure, whereby an
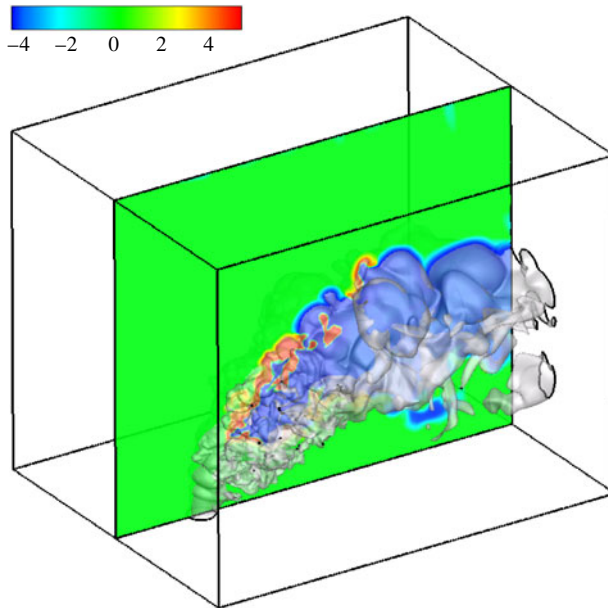
FIGURE 4. Illustration of CEMA t_{exp}^* field for reacting simulation. The translucent surface indicates stoichiometric mixture fraction; mean flow is from left to right, and the fuel jet enters from the bottom.

eigenvalue analysis of the chemical rate Jacobian is used to identify chemical modes that – in the absence of transport – would be expected to result in 'explosion', or transition to burning. Since transport is not included in the analysis, the results indicate where the *mixture preparation* is adequate to support combustion. This is consistent with conventional practice where the chemical time scale is determined from the reaction rate contributing to a 'key' species, without the difficulty that a single species can seldom represent all of the chemical time scales of interest.

From the procedure proposed by Lu *et al.* (2010), the eigenvalues of the chemical rate Jacobian $\boldsymbol{J}$ are obtained and the eigenvalue with the largest real part (excepting the eigenvalues with, for $n_{elements}$ elements appearing in the chemical mechanism, the smallest $[n_{elements} + 1]$ real part magnitudes for mass and energy conservation) is denoted by t_{exp}, reflecting the inverse time scale of the most explosive mode. The time scale is then normalized as

$$t_{exp}^* = \text{sign}(t_{exp}) \times \log_{10}[\max(1, |t_{exp}|(\text{s}^{-1}))]. \tag{3.1}$$

Lu *et al.* (2010) found the transition of t_{exp}^* from a positive to negative value clearly delineated the premixed or auto-igniting fronts in a lifted, auto-igniting, slot-jet flame DNS (Yoo *et al.* 2009).

The spatial variation of t_{exp}^* is shown in figure 4 for our present DNS on the mid-plane slice. In contrast to the DNS of Yoo *et al.* (2009), we do not see significantly positive values of t_{exp}^* immediately downstream of the jet exit; such 'ignitable' mixture preparations do not exist until significantly downstream of the jet exit due to the lower cross-stream temperature. That the mixture does not become ignitable until after the shear-layer-vortex development highlights the importance of shear layer vortices in mixture preparation. However, the regions where there is a transition from a

significantly positive t^*_{exp} to negative values is consistent with our expectations of premixed-like flame behaviour near the stabilization location in a sheet and in islands along the edges of the jet moving downstream. In our previous studies, where we used a combination of Takeno's flame index ($FI \equiv \nabla Y_F \cdot \nabla Y_O$; Y_F, Y_O are the mass fractions of the fuel and oxidizer species, respectively, here H_2, O_2) and heat-release contours to qualitatively identify premixed flame behaviour, we saw similar trends. The positive values of t^*_{exp} are found just ahead of the location of significant heat release; for $|t^*_{exp}| < 2.0$, the heat release is virtually non-existent. The region where $0 < t^*_{exp} < 2$ therefore identifies the 'preflame' region where the mixture preparation could support combustion, but burning has not taken place. Later, we will use the region where $t^*_{exp} > 1.0$ to demarcate the ignitable and leading edge of the burning portions of the domain. In later sections (§§ 4.2.1 and 4.2.2) we will revisit the positioning and nature of these regions within the jet plume.

3.2. *Jet trajectory parametrization*

Compared to configurations with an immediately apparent coordinate system for analysis, such as planes orthogonal to the jet axis in a co-flowing jet, the jet in cross-flow requires more thought. Su & Mungal (2004) discussed the jet trajectory in terms of the 'centreline' defined in several ways, one of which was based on 'the locus of points of maximum mean scalar concentration along trajectory-normal profiles'. For combustion, defining the jet trajectory with respect to a conserved scalar is eminently attractive. The scalar mixing is intimately connected to the combustion process, and links the jet/cross-flow interaction to the stabilization. Also, a conserved scalar can be defined even in the presence of the flame, whereas the other trajectories considered in the literature (e.g. the momentum trajectory or centre streamline; Muppidi & Mahesh 2005) are difficult to interpret in the presence of the dilatation from the combustion heat release and on an instantaneous basis for a turbulent jet.

   In defining the jet trajectory, our objective is to transform our three-dimensional space into a single jet coordinate that we can use to parametrize field quantities such as flame position, turbulence intensity, etc. Further complication is introduced due to seeking a volumetric parametrization defined throughout the interior of the jet and not just on the jet centreline: either the jet centreline trajectory must be extended to the outer bounds of the jet, or the jet boundary must be parametrized and extended to the interior. We chose the latter approach to accommodate the convoluted nature of the jet surface (and centreline) in the turbulent field. Extending the centreline throughout the jet interior by striking planes normal to the centreline, while feasible for the average jet trajectory, is not well suited to instantaneous trajectories. The uniqueness of the parameter value so assigned is only guaranteed on the centreline: off the centreline, the planes may intersect with each other. Tendrils of the jet that are highly curved are particularly susceptible to this, and to being assigned values in which the parametrization does not monotonically increase with distance along the jet surface.

   Alternatively, we obtain a jet path parametrization j based on the solution to Laplace's equation on a mixture fraction isosurface ($\xi = 0.05$) describing the outer boundary of the scalar jet. We first use a parallel implementation of the marching cubes algorithm (Lorensen & Cline 1987) to extract the isosurface *in situ* using cubes defined by the simulation grid. Subsequently, we merge the patches corresponding to each sub-domain into a continuous surface and we remove any small isolated surface components that are not a part of the main jet. To facilitate post-processing we simplify this surface from $O(10^7)$ to $O(10^5)$ triangles using QSlim (Garland & Heckbert 1997). This significantly reduces the computational cost of the subsequent
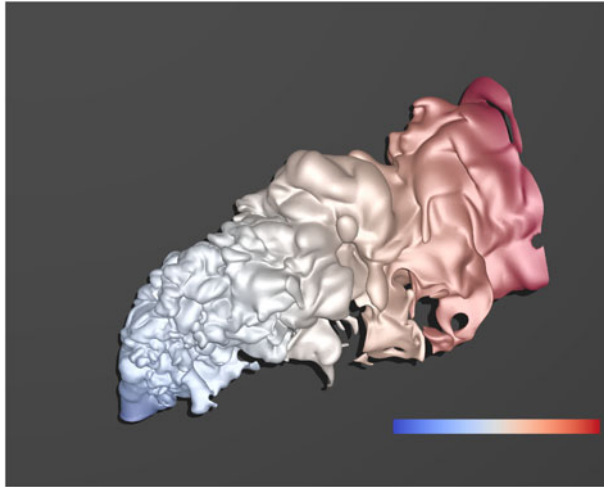
FIGURE 5. Variation of jet parametrization along the $\xi = 0.05$ isosurface from REJICF.

linear solves without markedly impacting the solution to Laplace's equation (Taubin 1995). One can then use any of the standard discrete formulations of Laplace's equation (Floater & Hormann 2005) to solve for j such that:

$$\nabla^2 j = 0, \tag{3.2}$$

with

$$\begin{aligned} j = 0 & \quad \forall y = 0, \\ j = 1 & \quad \forall x = L. \end{aligned} \tag{3.3}$$

This produces a parameter value that varies monotonically from 0.0 at the jet inlet to 1.0 at the jet exit along the surface, as shown in figure 5. Next, we generate a tetrahedral mesh of the jet interior starting from the surface triangles with TetGen (Si 2011). We assign boundary conditions from the surface solution and solve (3.2) on the interior using a volumetric finite-element formulation. In both the surface and interior cases we use SuperLU (Demmel *et al.* 1999) to solve the resulting system of equations for j. Finally, the values j from the tetrahedral mesh are interpolated onto the grid points of the original DNS solution. There are a number of existing interpolation techniques; for simplicity we compute the average j of the k closest tetrahedral vertices using the Approximate Nearest Neighbor library (ANN; Mount 2010). In practice, we have found that the jet trajectory obtained using $k = 2, 5, 10$ are indistinguishable, so we use $k = 2$ henceforth.

As a practical matter, the choice of the isosurface to delineate the outside edge of the jet and construct the parametrization is constrained to be as near to the edge of the jet as is numerically feasible. The parametrization is only defined inside the chosen surface (although we can extrapolate outside slightly), so we want to encompass as much of the jet as possible. The isosurface chosen must also exist continuously from the jet inlet to exit for the definition to be sensible. In light of these constraints, we could choose any reasonable mixture fraction isovalue near to, but larger than, $\xi = 0$. To assuage fears that parametrization might be sensitive to the isovalue chosen, we have tested the response of the computed jet trajectory for a range of isosurfaces
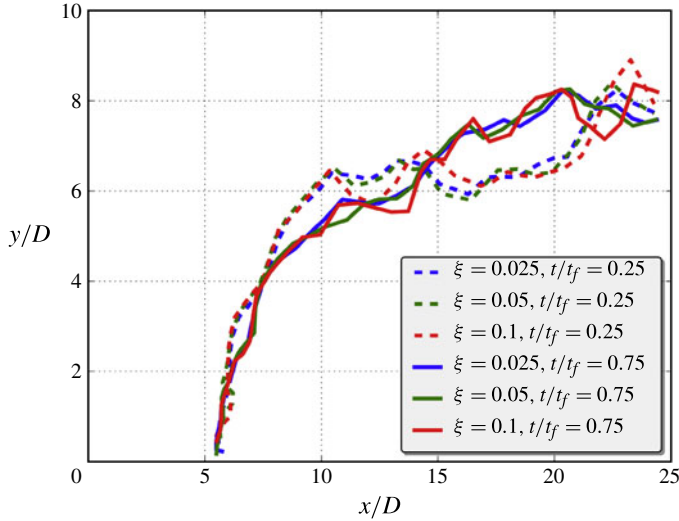
FIGURE 6. Comparison of jet trajectories from REJICF computed by applying jet path parametrization to isosurfaces defined by $\xi = 0.025, 0.5, 0.1$ at $t/t_f = 0.25, 0.75$.

at several instants in time. In figure 6, the computed trajectories are shown based on $\xi = 0.025, 0.05, 0.1$ for two times, $t/t_f = 0.25, 0.75$. The procedure for extracting a centreline trajectory from our parametrization is based on the same procedure we will use later to present the variation of key quantities along the jet trajectory. The conditional average of a given field variable a is denoted by $\langle a \mid j^* \rangle$, and is the average of the field $a(x)$ conditional on the field variable $j(x)$ taking the value j^*. Here, we compute the conditional averages $\langle \hat{x} \mid j^* \rangle$ and $\langle \hat{y} \mid j^* \rangle$, where $\hat{x}(x)$ and $\hat{y}(x)$ are field variables obtained from the x, y positions of each gridpoint. Figure 6 is generated by plotting the values of $\langle \hat{x} \mid j^* \rangle$ and $\langle \hat{y} \mid j^* \rangle$ together according to the values of the parameter j^* (we use 40 bins for j^*, so j^* varies from 0.0125 at the first point on the curve to 0.9875 at the final point). The sensitivity of the computed trajectory to the mixture fraction isovalue is negligible relative to the differences in the trajectory between the two times. In the remainder of this work, we have used the isosurface defined by $\xi = 0.05$ to define the jet parametrization.

4. Results

4.1. *Non-reacting jet trajectories*

Figure 7 compares the time-averaged jet trajectory (centre streamline) and the trajectory based on the jet path parametrization, from the non-reacting case NRJICF, to scaling laws from various authors given here in the general form

$$(y/R_m d) = A \times (x/R_m d)^b \times (h/d)^c, \tag{4.1}$$

to illustrate that the simulation behaves in a realistic manner. Values for the parameters A, b, h/d and c used by different authors are given in table 2. Samples of relevant quantities are accumulated throughout the computational domain for the non-reactive case NRJICF over a 4 ms window using 400 snapshots of the solution saved at 10 μs intervals. The total sampling window corresponds approximately to 11 transit times
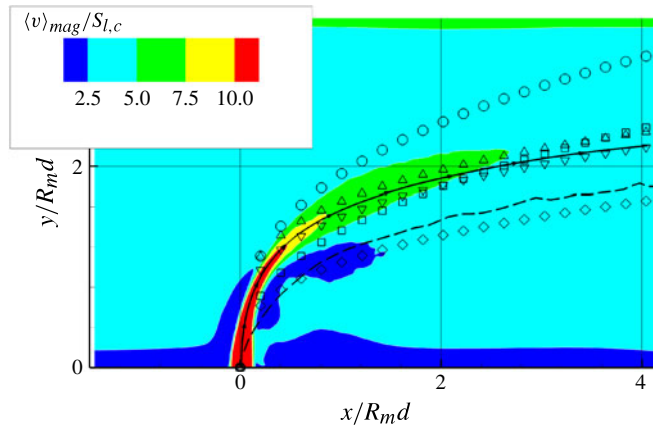
FIGURE 7. Jet trajectories from present non-reacting DNS (lines) compared with correlations from the open literature (symbols). The solid line indicates the centre streamline while the dashed line marks the jet scalar trajectory based on the jet path parametrization. Symbols: $\circ$ (centre streamline) and $\square$ (scalar wake trajectory), Su & Mungal (2004); $\triangledown$, Smith & Mungal (1998); $\triangle$, New *et al.* (2006); $\diamond$, Muppidi & Mahesh (2005). The coloured contours show the average velocity magnitude $\langle V \rangle_{mag}$ normalized by a relevant laminar flame speed $S_{l,c}$.

Author(s)	A	b	h/d	c
Su & Mungal (2004), centre streamline	1.92	0.342	0	0
Su & Mungal (2004), scalar wake	1.36	0.402	0	0
New *et al.* (2006)	1.65	0.250	0	0
Smith & Mungal (1998)	1.50	0.270	0	0
Muppidi & Mahesh (2005)	1.00	0.330	1.35	0.15

TABLE 2. Parameters used in (4.1) by different authors. The value of 1.35 for h/d is estimated in the present case by measuring the distance from the wall h of the centre streamline trajectory at a distance $x = 0.05d$ from the nozzle centre.

based on the free-stream velocity of the cross-flow and on the domain streamwise length; this corresponds to 226 d/U_{cf} time units and it includes more than 100 periods of the higher-frequency phenomena (shear layer vortices), approximately 50 periods of the slower processes (e.g. the turnover time for the CVP) and $\sim$10 periods of the slowest time scales associated with the wake structures. These estimates are well in accordance with the analysis provided in Bagheri *et al.* (2009), which indicates a tenfold increase of the characteristic time period for the wake vortical structures compared to the jet shear layer characteristic time. The trajectory indicated by the solid line is from the streamline exiting the nozzle centre, as suggested in Muppidi & Mahesh (2005), while the dashed line marks the trajectory based on the jet path parametrization. Notably, the centre streamline trajectory (a momentum-based curve, solid line) lies on the windward side of the trajectory obtained from the jet path parametrization (a scalar-based curve, dashed line). This is a common observation in the literature (see figure 20 in Su & Mungal 2004 as an example) that is confirmed by the present results. Furthermore, comparison with scalar trajectory correlations of the

form of (4.1) from earlier studies (open symbols) shows satisfactory agreement within the large amount of scatter typical for transverse jets configurations. Interestingly, the correlation that seems to best reflect the jet path parametrization trajectory is the scaling law suggested in Muppidi & Mahesh (2005) that, through the $(h/d)^c$ term, includes the effect of the jet velocity profile and of the boundary layer thickness on the jet scalar trajectory.

4.2. *Flame stabilization in fuel plume*

4.2.1. *Time-resolved behaviour*

The isosurfaces of the jet path parameter in figure 8 show that the heat-release rate begins to be noticeable on the trailing edge of the plume where the plume bends into the cross-flow, and along the upper edge after the plume is approximately aligned with the cross-flow. The heat release is highly asymmetric and rotates with respect to the plume over time in conjunction with a rotating mixture fraction field. The spatial fluctuations are much more uniformly distributed – the final isosurface shown has much less variation in all of the fields considered than the first – farther from the jet inlet, but still display remnants of the asymmetry evident near the inlet. The influence of the CVP can be seen in the shape of the jet plume, which evolves from the circular cross-section at the inlet to a marked horseshoe shape through the bend that eventually returns to an approximately circular shape when it exits the domain. This decay of the horseshoe shape affirms that our domain is long enough to capture the length scales associated with the key CVP.

The complexity of the flow structure interaction in the JICF configuration leads to a myriad of time scales ranging from the rapid local dissipation time scale associated with the intense strain from the shear between the jet and cross-flow to the extended oscillation of jet trajectory. As mentioned above, an estimate of the span between the shortest and the longest time scales associated with the main vortical structures of the transverse jet configuration is provided in Bagheri *et al.* (2009), and this suggests that one flow-through time of the present setup corresponds approximately to one wake time period. Fric & Roshko (1994) measured the Strouhal number St for the wake vortical structures for a large range of jet Reynolds numbers and velocity numbers. Although their experimental conditions were not identical to the case considered here, their data gives a range of $St = 0.05$–0.2. Extracting the corresponding frequencies within these bounds for our case, we obtain bounds on the wake frequency of 2750–11000 Hz, or a period of 0.364 ms down to 90.9 μs, respectively. This 'wake structure period' with the longest expected time scale of 0.364 ms, is comparable with one of flow-through time ~ 0.4 ms; therefore we expect a single event related to the wake structures within our data collection period.

We can observe the influence of the disparate time scales in the fluctuation of the flame position, and using the CEMA analysis outlined in § 3.1, we can construct a quantitative measure of the flame position. First, we compute the probability distribution function (p.d.f.) of the jet path parameter conditional on $t_{exp}^* > 1.0$. This gives the distribution of the location of the ignitable mixtures within the jet plume. In practice, this distribution is quite broad because some ignitable mixture is still present, typically up to $j \sim 0.6$; we take the first bin in j-space with significant ($p(j) > 0.01$; $p(j)$ is the computed p.d.f.) content as the (upstream) leading edge of the flame. In figure 9, the position of the flame obtained in this manner is plotted over time. Two features are evident. First, there is an oscillation of the flame position on a time scale of the order of one-third of t_{flow}, as well as smaller fluctuations on a much shorter time scale. Secondly, at $t/t_{flow} \sim 0.7$, there is a transition between the apparently metastable
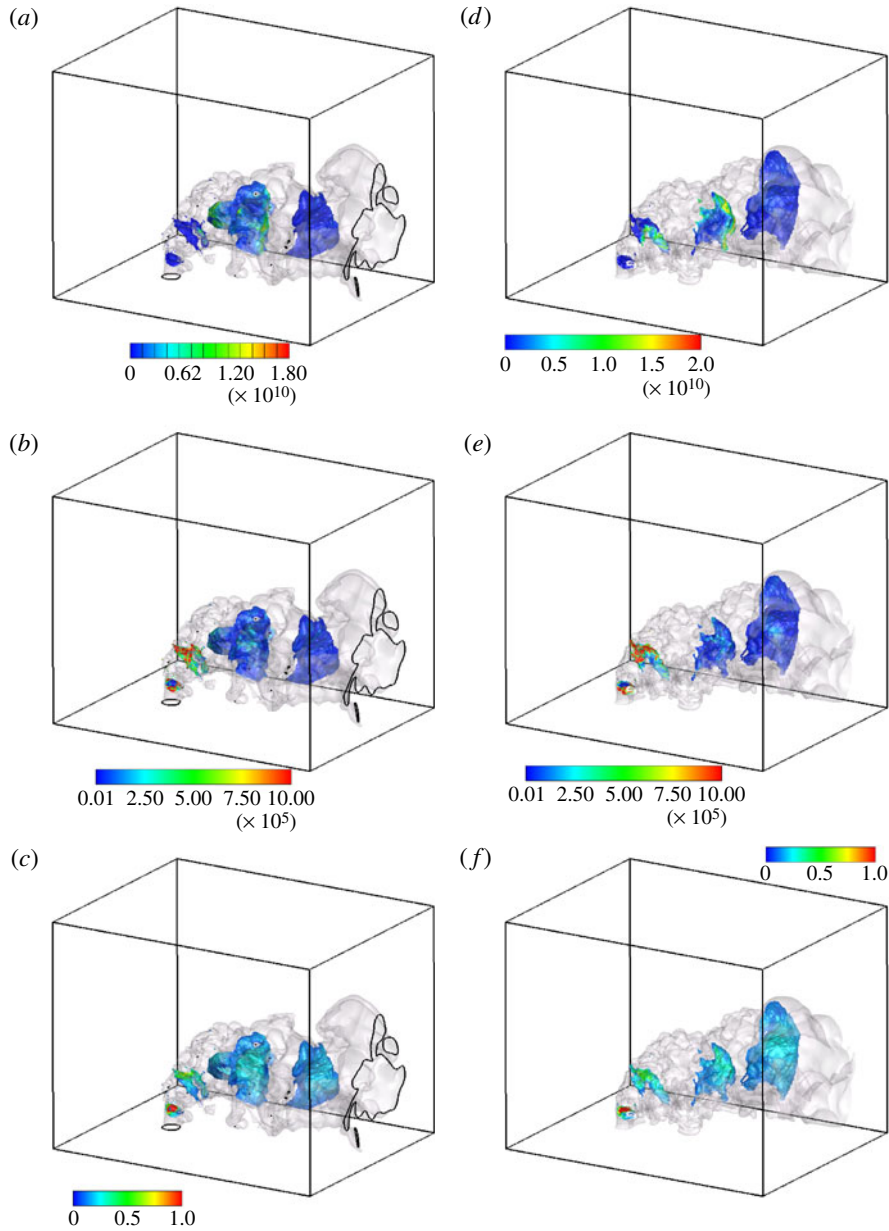
FIGURE 8. Isosurface of jet path parameter at $(a–c)$ $t/t_f = 0.25$ and $(d–f)$ $t/t_f = 0.75$, coloured by (a,d) heat-release rate (J m^{-3} s^{-1}), (b,e) vorticity magnitude (1 s^{-1}), and (c,f) mixture fraction. The translucent surface denotes $\xi = 0.05$; parametrization slices are at $j = (0.2, 0.4, 0.6, 0.8)$.

flame position seen in the earlier part of the data collection period and a second anchoring location that is much closer to the jet inlet. This event may be related to the wake vorticity time scale, which would explain why there is only a single occurrence within our data collection period.
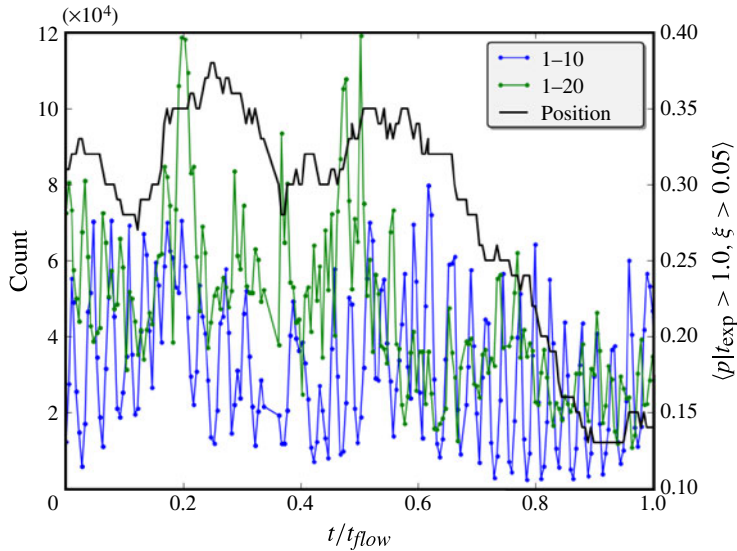
FIGURE 9. Instantaneous variation of flame position in jet plume and turbulence topology type above jet exit.

Figure 9 also shows a measurement of the vorticity from the jet shear layer based on the flow topological analysis of Chong, Perry & Cantwell (1990). In the analysis of an analogous square jet in cross-flow, Grout *et al.* (2011) observed that the vortices from the jet shear layer instability were clearly visible as instances of specific topological classifications. The count of the number of grid points with these indicator classifications within a small region on the leading edge of the jet $(4.5 < x/d < 5.5, \ 2.0 < y/d < 2.25, \ \forall z/d)$ is plotted alongside the flame position. The two chosen topological types correspond to flow configurations indicative of the strain-dominated arms of a well-defined vortex passing the sampling window. Clearly, the flame position fluctuates on a time scale far exceeding the frequency of jet shear layer vortex generation. In Grout *et al.* (2011), it seemed that the flame stabilization was phenomenologically related to the vorticity from the jet shear layer. However, figure 9 suggests that the time scales are disconnected, or at least that there is no trivial relationship between the observed effects.

The transition observed in figure 9 involves not only a movement towards the jet inlet by the most-upstream ignitable mixture, but also a change in the breadth of the heat-release rate. Figure 10 shows time-averaged mixture fraction, dissipation rate, vorticity magnitude, and heat-release rates over two short time windows before and during the transition. Before the transition, the heat release begins abruptly at $j \sim 0.4$ and is largely finished by $j \sim 0.8$. During the transition, the heat release still finishes by $j \sim 0.8$, but begins earlier at $j \sim 0.2$ and does not attain as high a peak. Interestingly, at the earlier time, there is a local peak in scalar dissipation rates just upstream of where the heat release begins, suggesting that perhaps there is a flow structure upstream of the flame with significantly high strain rates to prevent sustained burning, which decays and allows the flame to move upstream later in the simulation (interacting with vorticity and dissipation rates higher than in the first instance, but less than the 'barrier' structure).
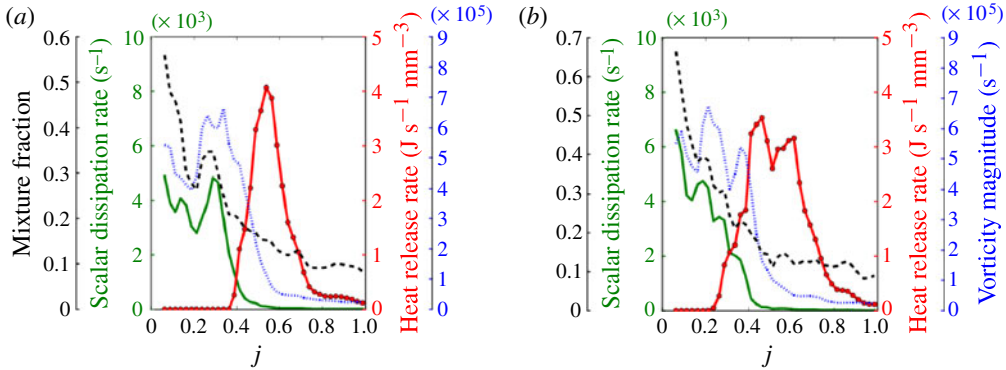
FIGURE 10. Short time conditional-averages centred on (*a*) $t/t_f = 0.25$ and (*b*) $t/t_f = 0.75$; averages include the indicated time snapshot bracketed by the sample at $t/t_f \pm 0.02$.
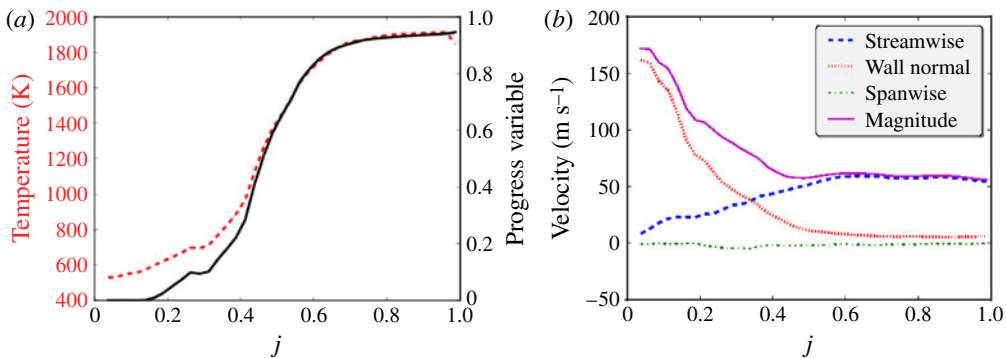

FIGURE 11. Time averages conditional on jet path parametrization.

Comparing figures 9 and 10, at both $t/t_{flow} = 0.25, 0.75$ we see the same sequence of events. Intense vorticity from shear layer vortices (from figure 10, at $j \approx 0.3, j \approx 0.2$, respectively) precedes appearance of significant positive t_{exp} (from figure 9 at $j \approx 0.37, j \approx 0.25$, respectively), corresponding to mixture prepared to explosive composition, shortly preceding the peak heat-release rate (again from figure 10).

4.2.2. *Time-averaged behaviour*

By conditionally averaging on j over an extended data collection period, we can quantify the time-average flame location. Figures 11 and 12 show averages for field variables within the jet ($\xi < 0.05$) conditional on the jet path parametrization. These averages are accumulated over a flow-through time based on the mean cross-flow velocity ($t = 0.4$ ms) comprising 202 evenly spaced, instantaneous snapshots of the flow. In figure 11, the flame position is indicated in terms of both temperature and a progress variable defined based on the H_2O mass fraction (Y_α is the mass fraction of species α) and the local mixture fraction:

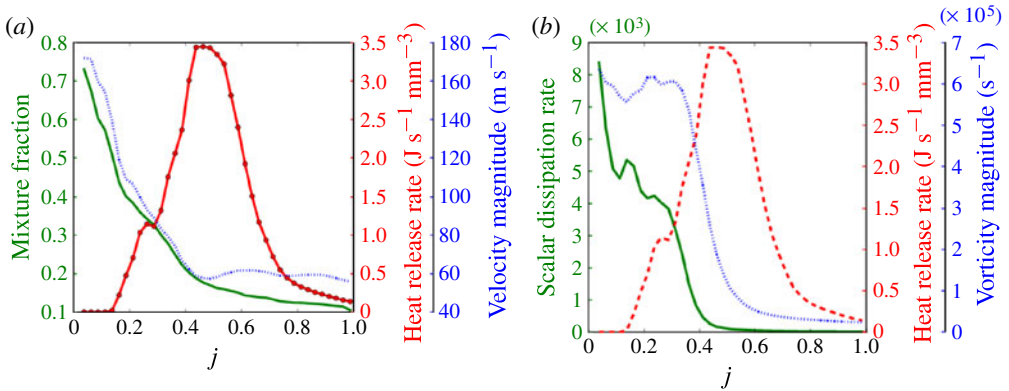$$c \equiv \frac{Y_{H_2O}}{Y_{H_2O,b}(\xi)}. \tag{4.2}$$

FIGURE 12. Time averages conditional on jet path parametrization.

This definition, as used by Poinsot *et al.* (1996) and Bray, Domingo & Vervisch (2005), accounts for changes in the fully burnt state due to mixing. Using this definition, the progress variable measure accentuates an interesting behaviour of the leading edge of the flame in figure 11(*a*): before the majority of the increase in progress variable near the jet parameter range 0.4–0.7, there is a local maximum near $j \approx 0.25$. In comparison to the conditionally averaged velocity components in figure 11(*b*), this maximum is just downstream of an inflection in the drop in the wall-normal velocity component as the jet bends over. This is definitely upstream, in the plume, of the majority of the progress variable increase, which is associated with a smooth decrease in the wall-normal average velocity along the jet and a corresponding increase in the streamwise average velocity. This transition is almost entirely complete by $j \approx 0.6$ on average. From the conditional velocity components, we can see that the jet 'bending' to align with the cross-flow is characterized by three distinct regions. During the first region, where approximately $j < 0.2$ – which we associate with the jet potential core – the wall-normal velocity drops rapidly and is not matched by a corresponding increase in the streamwise velocity. After a brief interruption, in the approximate range of $0.2 < j < 0.6$, the wall-normal velocity decreases again, but there is a corresponding increase in the streamwise velocity. Finally, for $j > 0.6$, the average wall-normal velocity is small and the streamwise velocity nearly constant. The peak – and majority – of the heat release occurs in the second of these regions: figure 12(*a*) shows the peak heat release just before $j \approx 0.5$, with a well-defined 'preflame' at $j = 0.25$. Interestingly, this 'preflame' heat release corresponds to the beginning of where the flame bends into the flow in the second region. The velocity magnitude from figure 11 is included in figure 12(*a*) for reference. From the mixture fraction, this region also seems to have relatively low rates of entrainment of oxidizer into the fuel jet. From figure 12(*b*), the mixture fraction scalar dissipation rate,

$$\chi \equiv 2D\nabla\xi \cdot \nabla\xi, \tag{4.3}$$

and enstrophy, defined relative to the magnitude of the local vorticity vector $\boldsymbol{\omega}$,

$$\Omega = 2\omega_{ij}\omega_{ij}, \quad \omega_{ij} = \frac{1}{2}\left(\frac{\partial u_i}{\partial x_j} - \frac{\partial u_j}{\partial x_i}\right), \tag{4.4}$$
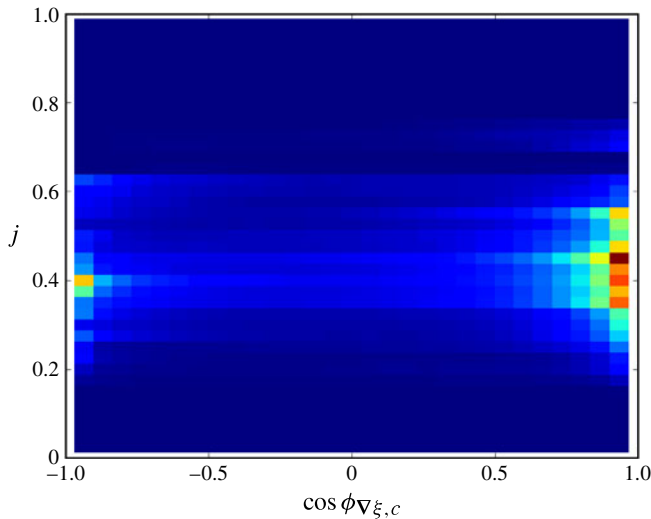
FIGURE 13. Alignment between $\nabla\xi$ and ∇c for an ignitable ($t_{exp} > 1.0$) mixture.

also display local elevations in this region. We note that the peak in vorticity in figure 12 is broader than the corresponding peak in χ_ξ. The rapid dissipation and drop in χ_ξ, taken together with the observations from the time-resolved data that explosive mixture preparation follows intense vorticity, suggests that turbulence *within the fuel plume* increases micro-mixing rates, is dominant relative to large-scale entrainment (which would be expected to significantly increase χ_ξ), and results in a sufficiently homogeneous mixture to support premixed (possibly distributed) combustion at the flame root. The lack of alignment in this region (figure 13) despite the existence of ∇c, $\nabla\xi$, indicates the absence of a clearly organized flame, i.e. distributed combustion. Further intense turbulence, which entrains the oxidizer from the cross-flow as the jet continues to bend towards the streamwise direction, appears to prepare the mixture for the peak heat release in the latter part of the bend region with a more clearly defined flame (progress variable and mixture fraction gradients are preferentially aligned for higher j).

The joint p.d.f. of alignment between the mixture fraction and progress variable gradients, $\nabla\xi$ and ∇c, in figure 13 for the ignitable portion of the domain, adds credibility to the scenario suggested above. At $j = < 0.25$, although ignitable mixture is present and both $\nabla\xi$ and ∇c exist, there is no clear alignment between the gradients, which suggests burning in a distributed mode, in the absence of a clearly organized flame. At $j \sim 0.4$, at the end of the bend from figure 11, there is significant volume where the flame is oriented parallel to the mixture fraction gradient, facing towards *richer* mixtures, i.e. facing towards the core of the plume, in what we referred to earlier as the flame root. Elsewhere within the approximate range $0.3 < j < 0.55$, across the peak heat-release rate from figure 12, $\nabla\xi$ and ∇c are predominantly aligned so that the flame faces towards leaner mixtures, consistent with a flame around the outside of the jet.
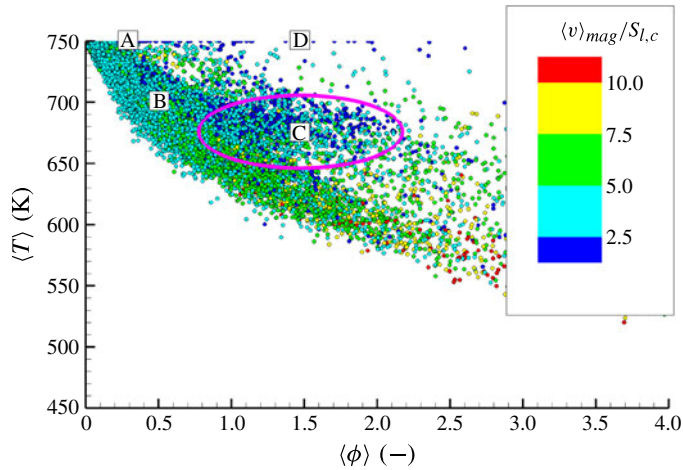
FIGURE 14. Scalar mixing for the NRJICF case illustrated by a scatter plot in $T - \phi$ space. The dots in the scatter plot are coloured by the locally averaged velocity magnitude normalized by the premixed laminar flame speed $S_{l,c}$ at position 'C'. The colour map is cropped to emphasize the points <2.5 (the full data range is 0–23.9). The pink ellipse indicates the probable flame root region.

Position	Temperature (K)	ϕ	S_l (m s^{-1})
A	750	0.3	3.2
B	700	0.5	5.5
C	675	1.5	11.4
D	750	1.5	12.6

TABLE 3. Computed laminar flame speeds for hydrogen–air mixtures at different temperatures and equivalence ratios.

4.2.3. *Anticipated flame stabilization from non-reacting baseline*

From the qualitative observations from Grout *et al.* (2011), we anticipate that the flame will anchor where the conditions are favourable in terms of both mixture preparation and sufficiently low dissipation rates.

The scatter plot in figure 14 shows the transverse jet mixing process in $\langle T \rangle - \langle \phi \rangle$ space where $\langle T \rangle$ is the local mixture average temperature and $\langle \phi \rangle$ the local mixture average equivalence ratio. Estimates for the laminar flame speed are obtained by the CHEMKIN PREMIX code (Kee *et al.* 1999) and given in table 3 for the reactants' preheat temperature and composition conditions marked by letters A–D in the diagram. The dots in the scatter plot are coloured by the local average velocity magnitude normalized by the laminar flame speed at position C ($S_{l,c}$) with a cropped colour map to emphasize the points where $\langle V \rangle_{mag}/S_{l,c} < 2.5$. The $\langle T \rangle - \langle \phi \rangle$ region near position C and delimited by the purple ellipse indicates a likely candidate for the flame root region: the simultaneous occurrence of local equivalence ratio $\langle \phi \rangle \sim 1.5$, relatively high mixture temperature $\langle T \rangle \sim 675$ K and relatively low average velocity magnitude (for many samples only 1–2 times larger than $S_{l,c}$) represents a favourable situation for aerodynamic anchoring and stabilization of the turbulent flame.
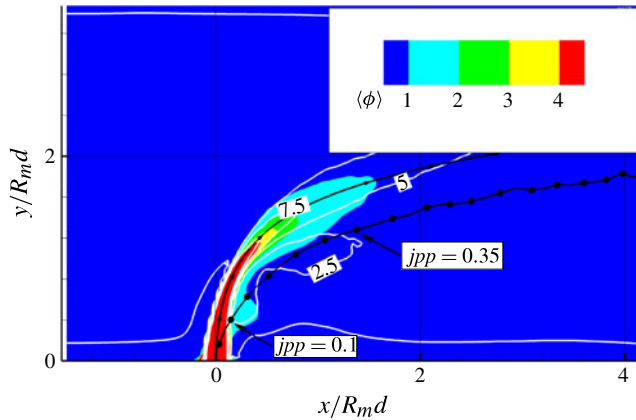
FIGURE 15. The time-averaged value of the equivalence ratio ϕ is represented by the coloured contours; the white isolines show the normalized average velocity magnitude normalized as in figure 7 while the black dotted line marks the jet trajectory based on the jet path parametrization.

The blue dots between locations A and D and beyond D correspond to fluid particles very close to the wall (i.e. below the quenching distance, $\langle V \rangle_{mag}/S_{l,c} = 0$) and therefore cannot support eventual flame stabilization due to heat loss. In physical space, the region corresponding to the possible anchoring position around location C in the $\langle T \rangle - \langle \phi \rangle$ diagram can be seen in figures 7 and 15. The coloured contours in figure 7 represent the averaged velocity magnitude field normalized by the laminar flame speed $S_{l,c}$; note the potential flame root region of relatively low speed (dark blue) just downstream of the jet trailing edge at approximately $y/R_m d \sim 1$ from the wall ($y/d \sim 3.5$), that is, the region of physical space that corresponds to the area around location C in figure 14. The potential flame root region created by the present mixing configuration is also marked by the white isocontour equal to 2.5 in figure 15, where the average hydrogen mass fraction is simultaneously shown, confirming the co-location of burnable mixture compositions and low velocities in the mean.

Figure 16 shows the joint p.d.f. of mixture fraction and velocity magnitude for the entire jet, conditional on being ignitable with significant heat release. For the dashed baseline, the most probable conditions are a lean mixture at slightly more than the mean cross-flow velocity. The solid p.d.f. is conditional on the flame anchoring regions: the restriction to $t^*_{exp} > 1.0$ removes the downstream flame body, while limiting to only the higher heat release separates potential from actual anchoring locations. Comparing the two distributions, the flame anchoring composition is on the lean side of stoichiometry, and there is a wide range of velocity magnitudes, including the low-velocity, near-stoichiometric region identified in the non-reacting jet.

The turbulence topological types used to count vortices in §4.2.1 are also useful to characterize the general nature of the flow as strain-dominated or rotation-dominated. The p.d.f. of topology types, gathered over the data collection period conditional on the jet path parameter (figure 17), indicates that the dominant topology as enumerated by Chong *et al.* (1990) changes along the plume. Early in the plume the node/saddle/saddle, unstable (type 12, strain-dominated) topology dominates, followed by focus/stretching, stable (type 18) topology. Downstream in the jet, the situation is reversed, with the focus/stretching, stable classification dominating, followed by
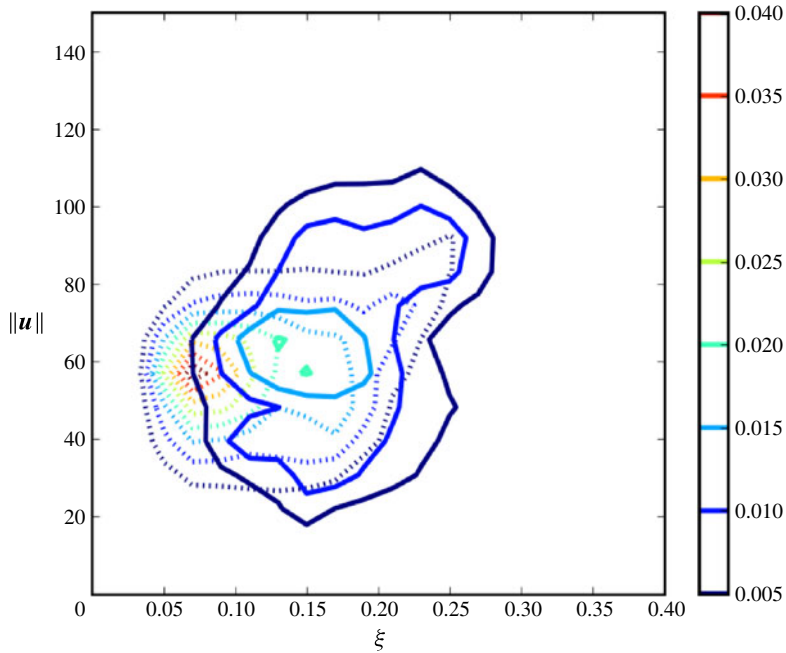
FIGURE 16. Joint p.d.f. of mixture fraction and velocity magnitude ($\|\boldsymbol{u}\|$) for entire domain (dotted) and portion of the domain with $t_{exp} > 1.0$, and heat-release rate exceeding 80 % of maximum (solid) for the transition period ($0.6 < t/t_f < 0.8$).
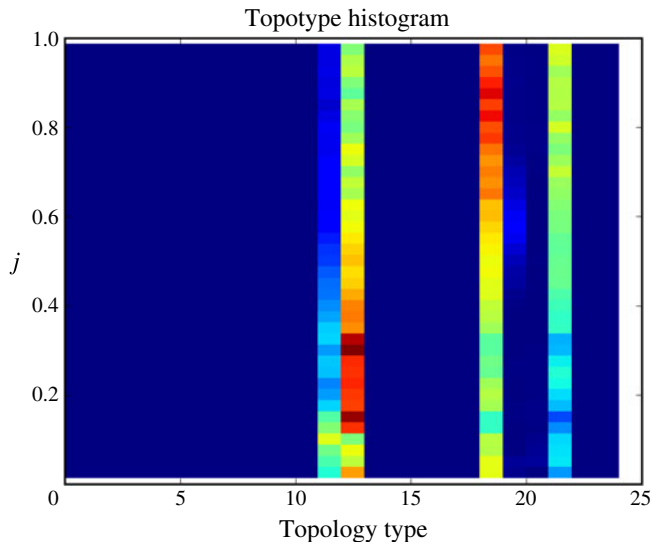

FIGURE 17. Conditional p.d.f. of turbulence topology variation along jet trajectory. Topology types are those enumerated by Chong *et al.* (1990); the significant classifications are 11 (node/saddle/saddle, stable), 12 (node/saddle/saddle, unstable), 18 (focus/stretching, stable), 19 (focus/stretching, unstable), 21 (focusing/compressing, unstable).

focusing/compressing, unstable. The location of this transition, $j \sim 0.4$, is in the j range identified earlier (figures 11 and 12 and the associated discussion) as where the jet bends, and where the flame stabilizes. This quantifies the transition from strain-dominated shear layer vortices, which provide rapid mixing, to flow topologies that favour recirculation and the occurrence of low velocity magnitude regions for stabilization.

4.3. *Flow and chemistry time scales*

With the vigorous turbulent structure, especially in the vicinity of the jet shear layer vortex breakdown, one might infer that turbulent mixing dominates the process. A reasonable characterization in this respect is vital for the selection of the appropriate modelling approach in, for example, a RANS simulation. Extremes in Damköhler number, $Da \equiv \tau_f/\tau_c$, where τ_f is a flow time scale and τ_c is a chemical time scale, indicate model formulations based on the thin flame (high Da) or distributed combustion (low Da) limits (Poinsot & Veynante 2001). Although conceptually straightforward, there is a great deal of subjectivity in choosing and evaluating the appropriate time scales for τ_c, τ_f (Veynante & Vervisch 2002), which have different interpretations for premixed versus non-premixed combustion modes. For our present interests, we require a *local* and *instantaneous* definition, so that we can inspect variation across the various regions in our configuration. We would also like to be able to collect statistics regarding the fluctuations in the time scale ratio that are of interest to various modelling efforts, such as those described in Oberlack, Arlitt & Peters (2000) and Pitsch & Fedotov (2001).

The scalar dissipation rate provides a useful local time scale for diffusive transport based on the scalar gradients (which may be influenced by the turbulent strain and/or reaction). Bray *et al.* (2005) identified three scalar dissipation rates that are potentially relevant in a partially premixed situation:

$$\chi_\xi = D\boldsymbol{\nabla}\xi \cdot \boldsymbol{\nabla}\xi, \tag{4.5}$$

$$\chi_c = D\boldsymbol{\nabla}c \cdot \boldsymbol{\nabla}c, \tag{4.6}$$

$$\chi_{\xi,c} = D\boldsymbol{\nabla}\xi \cdot \boldsymbol{\nabla}c. \tag{4.7}$$

For non-premixed combustion, only the first of these is pertinent, and has frequently been used to characterize the mixing time scale in the analysis of non-premixed DNS results (Swaminathan & Bilger 1997; Lu *et al.* 2010). In non-premixed flames, where turbulent strain acts to increase scalar gradients (Ashurst *et al.* 1987), this is a useful measure of the effects of turbulent strain. For premixed and partially premixed combustion, the latter two come into play. The progress variable gradients are not as clearly determined by the turbulent strain, but rather the result of complex interactions between reaction and turbulence. In some situations, premixed flame behaviour steepens the gradients and the velocity field dissipates them (Swaminathan & Grout 2006). In general, these measures are less useful for characterizing the flow time scales than in the non-premixed situation. The bulk flow time scale for premixed flames is typically estimated from the integral scale characteristics $\tau_f = l_t/u'$ (l_t being the integral length scale and u' the r.m.s. velocity fluctuation); the magnitude of the vorticity pseudo-vector provides a local analogue with a consistent interpretation for both premixed and non-premixed situations.

Conversely, the chemical time scale is more easily defined for premixed flames. In regimes that are clearly premixed, a chemical time scale can be defined based on the canonical structure, using the time for the flame to propagate over its own
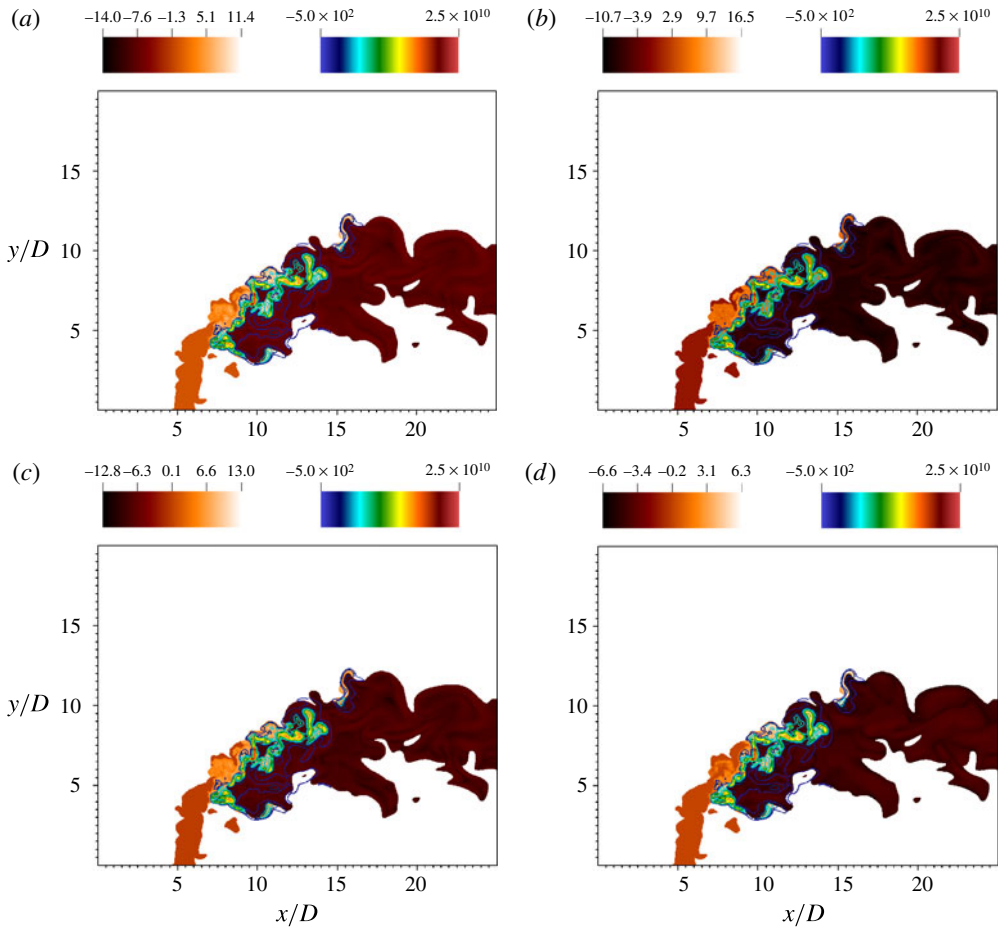
FIGURE 18. Local Damköhler numbers (colour map) based on chemical time scale from CEMA (t^*_{exp}) and flow time scale from (*a*) χ_ξ, (*b*) χ_c, (*c*) $\chi_{\xi c}$, and (*d*) vorticity magnitude with contours of heat-release rate.

thickness, whereas for non-premixed flames, there is as yet no clear agreement about the appropriate chemical time scale (Veynante & Vervisch 2002). In introducing the CEMA analysis described in §3.1, Lu *et al.* (2010) proposed to use the time scale associated with the dominant non-conservation mode. Large positive values of this mode (resulting in large, positive *Da*) imply rapid progression towards thermal runaway. Negative values of this mode (which lead to negative *Da* using this definition) correspond to 'burnt' regions that require further mixing to move towards thermal runaway. This distinction is possible because the CEMA modes are purely thermochemical: transport is not included in the eigenvalue analysis.

In figure 18, the Damköhler number is shown on a spanwise slice through the middle of the domain using the CEMA time scale to define τ_c. Unlike in the DNS of Yoo *et al.* (2009), where there was an obvious choice of scalar mixing time scale due to the non-premixed nature, here we have premixed and partially premixed behaviour, which provides multiple options. Our options include obtaining the flow time scale from the three gradient-based scalar dissipations from (4.5)–(4.7), and the
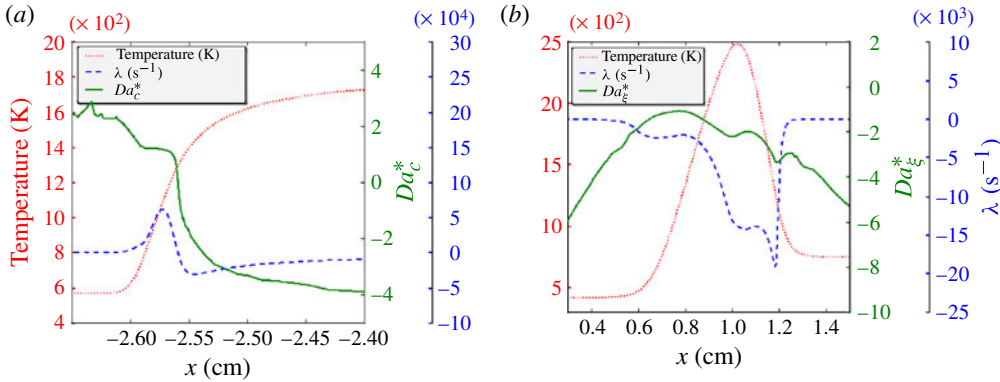
FIGURE 19. Explosive mode time scales (λ is the explosive mode corresponding to t_{exp} referred to elsewhere) and resulting Da^* for (a) freely propagating premixed and (b) strained opposed jet flames. The conditions correspond to fuel and air streams from DNS, in stoichiometric mixture for premixed case. The opposed jet solution velocities are $1\,\mathrm{m\,s^{-1}}$. Da_ξ^* and Da_c^* are computed according to (4.8) and (4.9).

vorticity magnitude, to indicate the relative time scales of the chemistry, along with the following.

(i) Mixing between the fuel and oxidizer:

$$Da_\xi^* = \operatorname{sign}(t_{exp}) \times \log_{10}[\max(1, |t_{exp} \cdot \chi_\xi^{-1}|)]. \tag{4.8}$$

(ii) Mixing between products and reactants:

$$Da_c^* = \operatorname{sign}(t_{exp}) \times \log_{10}[\max(1, |t_{exp} \cdot \chi_c^{-1}|)]. \tag{4.9}$$

(iii) Mixing affecting both product/reactants and fuel/oxidizer:

$$Da_{\xi c}^* = \operatorname{sign}(t_{exp}) \times \log_{10}[\max(1, |t_{exp} \cdot \chi_{\xi c}^{-1}|)]. \tag{4.10}$$

(iv) The local mechanical turbulence time scale (d) based on the magnitude of the vorticity vector $\boldsymbol{\omega}$:

$$Da_\omega^* = \operatorname{sign}(t_{exp}) \times \log_{10}[\max(1, |t_{exp} \cdot |\boldsymbol{\omega}|^{-1}|)]. \tag{4.11}$$

In light of the alignment between $\nabla\xi$ and ∇c discussed in §4.2.2, it is perhaps unsurprising that the first three time scale ratios have similar magnitude and qualitative structures. For all three dissipation rate measures, the local Da within the burning region is of order 10^1, with the vorticity-based measure lower by approximately half. The negative time scale ratios arise because the sign resulting from the CEMA eigenvalue magnitude has been retained: where this is negative indicates a mixture that is thermochemically 'burnt', and although reactions may still be occurring, it will not proceed to thermal runaway in isolation. This is illustrated by considering the analysis applied to canonical one-dimensional premixed (figure 19a) and non-premixed (figure 19b) flames. In the preheat region of a premixed flame the explosive mode, and hence Da_c^*, is positive, of order 10–100, indicating that even in the absence of any mixing the state will eventually proceed to burning. In the non-premixed flame, we see
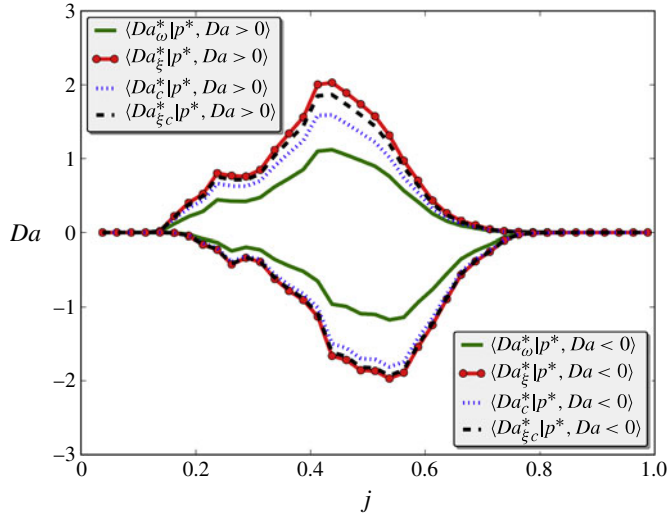
FIGURE 20. Time-averaged Da^* conditional on jet position. Conditional averages are computed separately for positive and negative modes.

the other case, where the mixture results in a negative explosive mode (as expected: mixing is necessary for further reaction progress), with Da_ξ having smaller magnitude in the mixing zone. When the stream velocities in the opposed jet were increased to near extinction (32 m s^{-1}), the most negative Da in the mixing layer decreased significantly ($Da^* \approx -6$ at the edges of the mixing region, compared to $Da^* \approx -2$ at the edges of the mixing layer for the low-strain case in figure 19). By collecting time averages separately for the positive and negative regions conditional on j, we see in figure 20 that the largest positive average Da is reached slightly ahead of the largest negative average Da at $j = 0.45$ and $j = 0.55$, respectively. Within the range of j identified earlier as encompassing the bulk of the heat release, we have $Da > 1$, indicating that chemistry occurs faster than mixing, but not in the limit $Da \gg 1$, which would suggest a thin flame regime. This is consistent with the qualitative sense we obtain from cross-sections through the flame where the width of the heat-release zone is smaller than, but comparable to, the apparent size of the vortical structures. In the range of j where we identified a 'preflame', the average $Da < 10$ supports our earlier identification of distributed reaction in a well-mixed zone subjected to intense turbulence. To put the Da ranges from this metric in context, it should be recalled that for purely premixed flames, a traditional local Da measure is the ratio of the species reaction term to diffusion term. In the non-premixed jet flame studied by Lu *et al.* (2010), the Favre conditional mean Da based on H_2O varied between ~ 1 and 20 with much larger (0–110) variance, and the range of the Da defined as in (4.8) was ± 54.

4.4. *Turbulence structure and effects*

4.4.1. *Turbulent strain alignment with scalar gradients*

Within a flame where the Damköhler number is moderate it is not yet well established if the turbulent strain will act to steepen or dissipate the scalar gradients; this has important implications for modelling, especially in RANS contexts. Swaminathan & Grout (2006) analysed high DNS of premixed flames in the high-Da regime and determined that the correlation between the progress variable gradients and
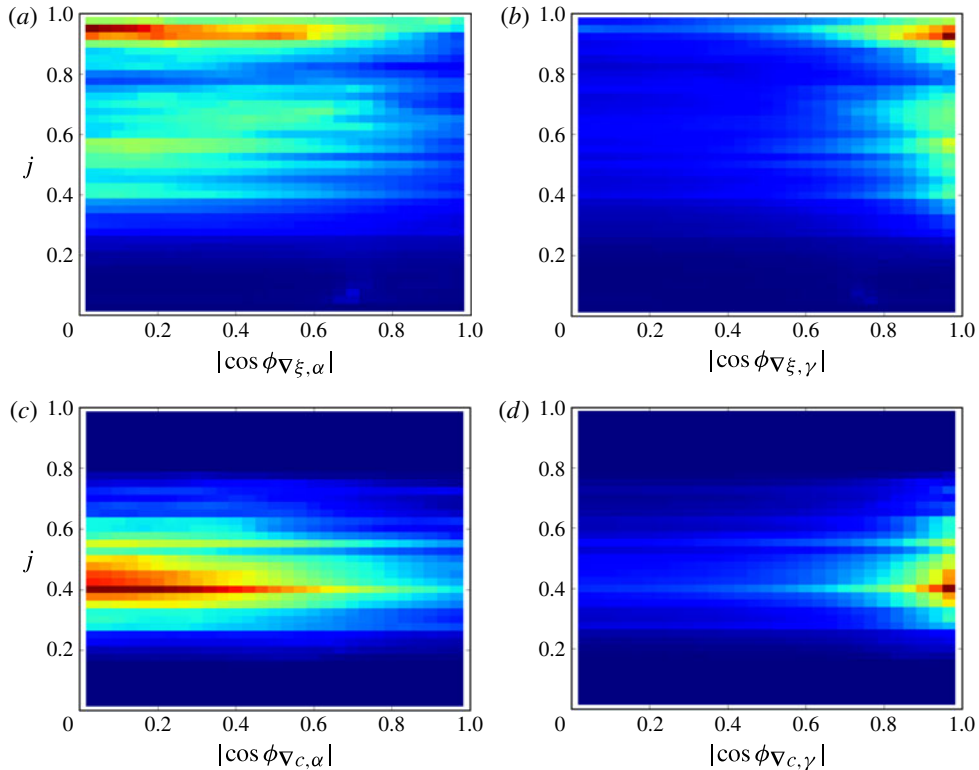
FIGURE 21. Joint p.d.f. of cosine of angle between mixture fraction gradient (*a,b*) or progress variable gradient (*c,d*) and most extensive (*a,c*) or most compressive (*b,d*) principal strain for the portion of the domain with significant heat release.

turbulent strain,

$$\frac{\partial c}{\partial x_i}\left(\frac{\partial u_i}{\partial x_j}+\frac{\partial u_j}{\partial x_i}\right)\frac{\partial c}{\partial x_j}, \tag{4.12}$$

on average has a negative value representing production of scalar gradients through preferential alignment between the scalar gradient and the most compressive strain in homogeneous flows for a passive scalar (Batchelor 1959; Gibson 1968; Kerr 1985), but has a *positive* value in some premixed flames. The positive case arises where the interaction between the heat-release-induced dilatation and the background turbulence results in a preferential alignment between the scalar gradients and the most extensive turbulent strain. Since this flame clearly does not fall within the high-*Da* or low-*Da* limits, it is appropriate to check if there is a preferential alignment between the scalar gradients and the compressive/extensive strains to determine the expected results of the turbulence–chemistry interaction. In figure 21, we have computed the distribution of the cosine of the angle between the scalar gradients and the most extensive (α) and most compressive (γ) turbulent strains conditional on the jet path parameter for the portion of the domain where the heat-release rate is significant (>80 % of the maximum). Since the effect we are looking for is caused by heat-release-induced dilatation, the last condition ensures that the effect is not masked by the balance of the domain away from the heat-release zone. For both the mixture

fraction and progress variable gradients, and throughout the jet, we see a clear preferential alignment between the scalar gradient and the most compressive strain, with an associated preferential orthogonality between the scalar gradients and the most extensive strain. This suggests that in this regime, where $1 < Da \lll \infty$, the turbulence–scalar interaction follows the classical expectation that turbulent strain acts to increase scalar gradients, consistent with the findings of Chakraborty & Swaminathan (2007) for premixed flames with single-step chemistry at moderate and large Da.

4.4.2. *Counter-gradient diffusion*

Concluding the present section, we explore the magnitude of counter-gradient diffusion due to the Reynolds scalar fluxes $\langle u'c' \rangle$ in the NRJICF dataset. The occurrence of counter-gradient diffusion of the turbulent scalar fluxes on the scale observed in the non-reacting case poses a serious modelling challenge, and could explain the poor predictions obtained by RANS and LES methods that rely on the gradient assumption in reproducing the Reynolds scalar fluxes measured in JICF scalar mixing configurations such as Galeazzo *et al.* (2011). We leave development of effective techniques to account for these phenomena, and assessment against the reacting flow dataset, for future endeavours.

Figure 22 reveals and quantifies the occurrences, showing the surfaces of negative eddy diffusion coefficients for the three spatial directions. The scalar c is the mass fraction of hydrogen, Y_{H2}, and the Reynolds scalar fluxes in figure 22(*b–d*) are normalized by the cross-flow velocity, U_{cf}, multiplied by the hydrogen mass fraction at the jet nozzle exit, $Y_{H2,jet}$. The presence of counter-gradient diffusion in transverse jets has been recently discussed in Muppidi & Mahesh (2008), although that analysis is restricted to a limited region of the jet symmetry plane and reports significant counter-gradient diffusion in the wall-normal and spanwise directions only. The present results indicate large regions of counter-gradient diffusion also outside the symmetry plane, on the side of the jet trajectory and in its wake, involving all spatial directions.

5. Conclusions

Through detailed simulations and analysis using a global parametrization of non-reacting and reacting jet in cross-flow configurations, it is apparent that the complexity of the flow structure in this configuration results in rich flame behaviour that will likely pose a significant challenge for approximate calculations employing models for unresolved effects. Tendrils of the flame upstream of the bulk of the heat-release rate penetrate into intense vorticity from the jet shear layer, which acts on a relatively short time scale, while the bulk flame position is modulated by relatively long time scale events in the jet wake. In general, although the flame position is unsteady, the peak heat release coincides with the location where the jet vortex breakdown occurs and the jet bends to align with the cross-flow direction. Along with the position of the flame root, the breadth of the heat release is unsteady. Particularly strong vorticity and velocity magnitudes appear to present a barrier to upstream flame propagation, but result in a mixture preparation that burns in a more confined region when the intensity decays. Throughout the jet, the flame is oriented such that progress variable and mixture gradients are parallel, both preferentially aligned with the most compressive turbulent strain. This is favourable for turbulence models that include a source for scalar gradients due to turbulence; however, significant counter-gradient diffusion is observed, which represents a challenge for turbulence models employing a gradient-diffusion assumption to close the velocity-scalar fluctuation correlation terms,
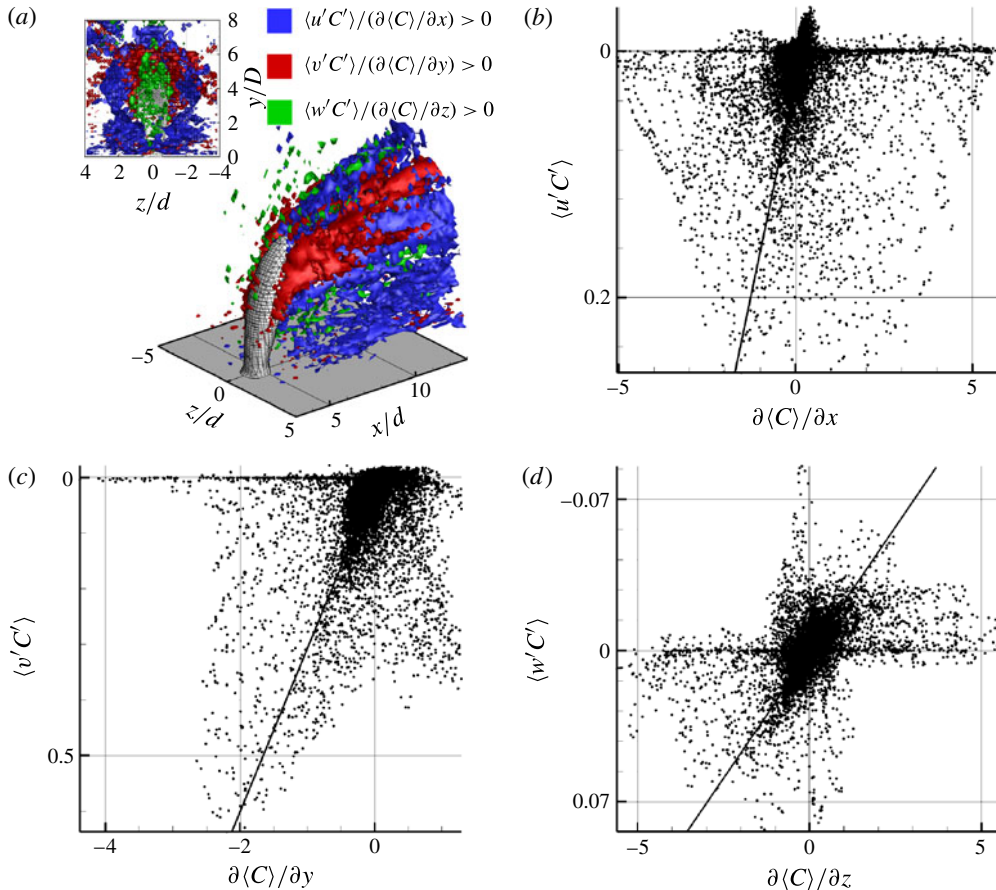
FIGURE 22. Spatial regions of counter-gradient scalar diffusion in x-, y- and z-direction, shown by blue, red and green isosurfaces, respectively (a). The white meshed surface indicates the average hydrogen mass fraction, $Y_{H_2} = 0.01$, and is used to mark the jet flow in the figure. The scatter plots show the variation of the Reynolds scalar fluxes with the mean scalar gradients in x- (b), y- (c), and z-direction (d). The solid lines mark the least square fit for the eddy diffusivity in the three coordinate directions.

and further work in this area would be beneficial. On average, topological analysis suggests that the turbulence within the jet plume is strain-dominated before the bend (jet approximately orthogonal to the wall) and rotation-dominated after the bend when the plume is oriented along the cross-flow direction. Finally, analysis of the location of flame stabilization in the reacting case suggests that the flame root is located in a region of relatively mild velocity magnitude and mixture flammability, a condition which would be expected from non-reacting simulations.

Acknowledgements

REFERENCES

ANDREOPOULOS, J. 1985 On the structure of jets in a crossflow. *J. Fluid Mech.* **157**, 163–197.

ANDREOPOULOS, J. & RODI, W. 1984 Experimental investigation of jets in a crossflow. *J. Fluid Mech.* **138**, 93–127.

ASHURST, W. T., KERSTEIN, A. R., KERR, R. M. & GIBSON, C. H. 1987 Alignment of vorticity and scalar gradient with strain rate in simulated Navier–Stokes turbulence. *Phys. Fluids* **30**, 2343–2353.

BAGHERI, S., SCHLATTER, P., SCHMID, P. J. & HENNINGSON, D. S. 2009 Global stability of a jet in crossflow. *J. Fluid Mech.* **624**, 33–44.

BATCHELOR, G. K. 1959 Small scale variations of convected quantities like temperature in turbulent fluid. Part 1. General discussion and the case of small conductivity. *J. Fluid Mech.* **5**, 113–133.

BRAY, K. N. C., DOMINGO, P. & VERVISCH, L. 2005 Role of the progress variable in models for partially premixed turbulent combustion. *Combust. Flame* **141**, 431–437.

BROADWELL, J. E. & BREIDENTHAL, R. E. 1984 Structure and mixing of a transverse jet in incompressible flow. *J. Fluid Mech.* **148**, 405–412.

BRZUSTOWSKI, T. A., GOLLAHALLI, S. R. & SULLIVAN, H. F. 1975 The turbulent hydrogen diffusion flame in a cross-wind. *Combust. Sci. Technol.* **11**, 29–33.

CHAKRABORTY, N. & SWAMINATHAN, N. 2007 Influence of the Damköhler number on turbulence–scalar interaction in premixed flames. Part 1. Physical insight. *Phys. Fluids* **19**, 045103.

CHEN, J. H., CHOUDHARY, A., DE SUPINSKI, B., DEVRIES, M., HAWKES, E. R., KLASKY, S., LIAO, W. K., MA, K. L., MELLOR-CRUMMEY, J., PODHORSKI, N., SANKARAN, R., SHENDE, S. & YOO, C. S. 2009 Terascale direct numerical simulations of turbulent combustion using S3D. *Comput. Sci. Disc.* **2**, 1–31.

CHONG, M. S., PERRY, A. E. & CANTWELL, B. J. 1990 A general classification of three-dimensional flow fields. *Phys. Fluids* A **2** (5), 765–777.

COELHO, S. L. V. & HUNT, J. C. R. 1989 The dynamics of the near field of strong jets in crossflows. *J. Fluid Mech.* **200**, 95–120.

CORTELEZZI, L. & KARAGOZIAN, A. R. 2001 On the formation of the counter-rotating vortex pair in transverse jets. *J. Fluid Mech.* **446**, 347–373.

DEMMEL, J. W., EISENSTAT, S. C., GILBERT, J. R., LI, X. S. & LIU, J. W. H. 1999 A supernodal approach to sparse partial pivoting. *SIAM J. Matrix Anal. Appl.* **20** (3), 720–755.

DÖBBELING, K., HELLAT, J. & KOCH, H. 2007 25 years of BBC/ABB/Alstom lean premix combustion technologies. *ASME J. Engng for Gas Turbines and Power* **129**, 2–12.

ECHEKKI, T. & CHEN, J. H. 2003 Direct numerical simulation of autoignition in non-homogeneous hydrogen–air mixtures. *Combust. Flame* **134**, 169–191.

FEARN, R. & WESTON, R. 1974 Vorticity associated with a jet in a cross flow. *AIAA J.* **12**, 1666–1671.

FEARN, R. L. & WESTON, R. P. 1975 Induced pressure distribution of a jet in a crossflow. *Tech. Rep.* TN-D7916. NASA, Langley Research Center.

FEARN, R. L. & WESTON, R. P. 1978 Induced velocity field of a jet in a crossflow. *Tech. Rep.* TP-1087. NASA, Langley Research Center.

FEARN, R. L. & WESTON, R. P. 1979 Velocity field of a round jet in a cross flow for various jet injection angles and velocity ratios. *Tech. Rep.* TP-1506. NASA, Langley Research Center.

FLOATER, M. & HORMANN, K. 2005 Surface parameterization: a tutorial and survey. In *Adv. Multiresolution for Geometric Modelling*, pp. 157–186. Springer.

FRIC, T. F. & ROSHKO, A. 1994 Vortical structure in the wake of a transverse jet. *J. Fluid Mech.* **279**, 1–47.

GALEAZZO, F. C. C., DONNERT, G., HABISREUTHER, P., ZARZALIS, N., VALDES, R. J. & KREBS, W. 2011 Measurements and simulation of turbulent mixing in a jet in crossflow. *ASME J. Engng Gas Turbines and Power* **133**, 061504.

GARLAND, M. & HECKBERT, P. S. 1997 Surface simplification using quadric error metrics. In *Proceedings of the 24th Annual Conference on Computer graphics and Interactive Techniques: SIGGRAPH'97*, pp. 209–216. Association for Computing Machinery, Inc. (ACM).

GIBSON, C. H. 1968 Fine structure of scalar fields mixed by turbulence. Part 1. Zero gradient points and minimal gradient surfaces. *Phys. Fluids* **11**, 2305.

GOLLAHALLI, S. R. & PARDIWALLA, D. 2002 Comparison of the flame characteristics of turbulent circular and elliptic jets in a crossflow. *ASME J. Energy Resour. Technol.* **124**, 197–203.

GROUT, R. W., GRUBER, A., YOO, C. S. & CHEN, J. H. 2011 Direct numerical simulation of flame stabilization downstream of a transverse fuel jet in cross-flow. *Proc. Combust. Inst.* **33** (1), 1629–1637.

GRUBER, A., SANKARAN, R., HAWKES, E. R. & CHEN, J. H. 2010 Turbulent flame–wall interaction: a direct numerical simulation study. *J. Fluid Mech.* **658**, 5–32.

GUTMARK, E. J., IBRAHIM, I. M. & MURUGAPPAN, S. 2008 Circular and noncircular subsonic jets in cross flow. *Phys. Fluids* **20**, 075110.

HASSELBRINK, E. F. & MUNGAL, M. G. 2001*a* Transverse jets and jet flames. Part 1. Scaling laws for strong transverse jets. *J. Fluid Mech.* **443**, 1–25.

HASSELBRINK, E. F. & MUNGAL, M. G. 2001*b* Transverse jets and jet flames. Part 2. Velocity and OH field imaging. *J. Fluid Mech.* **443**, 27–68.

HAVEN, B. A. & KUROSAKA, M. 1997 Kidney and anti-kidney vortices in crossflow jets. *J. Fluid Mech.* **352**, 27–64.

HAWKES, E. R. & CHEN, J. H. 2005 Evaluation of models for flame stretch due to curvature in the thin reaction zones regime. In *30th International Symposium on Combustion*, pp. 647–655. The Combustion Institute.

HAWKES, E. R., SANKARAN, R., SUTHERLAND, J. C. & CHEN, J. H. 2007 Scalar mixing in direct numerical simulations of temporally evolving plane jet flames with skeletal CO/H_2 kinetics. In *31st International Symposium on Combustion*, pp. 1633–1640. The Combustion Institute.

HOLDEMAN, J. D. 1972 Correlation for temperature profiles in the plane of symmetry downstream of a jet injected normal to a crossflow. *Tech. Rep.* TN-D6966. NASA, Lewis Research Center.

JESSEN, W., SCHRÖDER, W. & KLAAS, M. 2007 Evolution of jets effusing from inclined holes into crossflow. *Intl J. Heat Fluid Flow* **28**, 1312–1326.

JIMÉNEZ, J., HOYAS, S., SIMENS, M. P. & MIZUNO, Y. 2010 Turbulent boundary layers and channels at moderate Reynolds numbers. *J. Fluid Mech.* **657**, 335–360.

KARAGOZIAN, A. R. 2010 Transverse jets and their control. *Prog. Energy Combust. Sci.* **36**, 531–553.

KEE, R. J., DIXON-LEWIS, G., WARNATZ, J., COLTRIN, M. E., MILLER, J. A. & MOFFAT, H. K. 1999 A Fortran chemical kinetics package for the analysis of gas-phase chemical kinetics. *Tech. Rep.* Release 3.5. Reaction Design Inc., San Diego, CA.

KELSO, R. M., LIM, T. T. & PERRY, A. E. 1996 An experimental study of round jets in crossflow. *J. Fluid Mech.* **306**, 111–144.

KENNEDY, C. A. & CARPENTER, M. H. 1994 Several new numerical methods for compressible shear-layer simulations. *Appl. Numer. Math.* **14** (4), 397–433.

KENNEDY, C. A., CARPENTER, M. H. & LEWIS, R. M. 2000 Low-storage, explicit Runge–Kutta schemes for the compressible Navier–Stokes equations. *Appl. Numer. Math.* **35** (3), 177–219.

KERR, R. M. 1985 Higher-order derivative correlations and the alignment of small-scale structures in isotropic numerical turbulence. *J. Fluid Mech.* **153**, 31–58.

LI, J., ZHAO, Z., KAZAROV, A. & DRYER, F. L. 2004 An updated comprehensive kinetic model of hydrogen combustion. *Intl J. Chem. Kinet.* **36**, 566–575.

LORENSEN, W. E. & CLINE, H. E. 1987 Marching cubes: a high resolution 3D surface construction algorithm. *Comput. Graph.* **21** (4), 163–169.

LU, T. F., YOO, C. S., CHEN, J. H. & LAW, C. K. 2010 Three-dimensional direct numerical simulation of a turbulent lifted hydrogen jet flame in heated coflow: a chemical explosive mode analysis. *J. Fluid Mech.* **652**, 45–64.

LUND, T. S., SQUIRES, K. D. & WU, X. 2003 Turbulent inflow boundary conditions for LES. In *Proceedings of the 41st Aerospace Sciences Meeting and Exhibit, 6–9 January 2003, Reno, Nevada*. American Institute of Aeronautics and Astronautics.

MOSER, R., KIM, J. & MANSOUR, N. 1999 Direct numerical simulation of turbulent channel flow up to $Re_\tau = 590$. *Phys. Fluids* **11** (4), 943–945.

MOUNT, D. M. 2010 *ANN Programming Manual*. http://www.cs.umd.edu/~ mount/ANN/Files/1.1.2/ ANNmanual_1.1.pdf.

MUPPIDI, S. & MAHESH, K. 2005 Study of trajectories of jets in crossflow using direct numerical simulations. *J. Fluid Mech.* **530**, 81–100.

MUPPIDI, S. & MAHESH, K. 2008 Direct numerical simulation of passive scalar transport in transverse jets. *J. Fluid Mech.* **598**, 335–360.

NEW, T. H., LIM, T. T. & LUO, S. C. 2006 Effects of jet velocity profiles on a round jet in cross-flow. *Exp. Fluids* **40**, 859–875.

OBERLACK, M., ARLITT, R. & PETERS, N. 2000 On stochastic Damköhler number variations in a homogeneous flow reactor. *Combust. Theor. Model.* **4** (4), 495–509.

PASSOT, T. & POUQUET, A. 1987 Numerical simulation of compressible homogeneous flows in the turbulent regime. *J. Fluid Mech.* **181**, 441–466.

PITSCH, H. & FEDOTOV, S. 2001 Investigation of scalar dissipation rate fluctuations in non-premixed turbulent combustion using a stochastic approach. *Combust. Theor. Model.* **5** (1), 41–57.

POINSOT, T. & LELE, S. K. 1992 Boundary conditions for direct simulations of compressible viscous flow. *J. Comput. Phys.* **101**, 104–129.

POINSOT, T. & VEYNANTE, D. 2001 *Theoretical and Numerical Combustion*, first edition. Edwards.

POINSOT, T., VEYNANTE, D., TROUVÉ, A. & RUETSCH, G. R. 1996 Turbulent flame propagation in partially premixed flames. *CTR Summer Program 1996*.

SALEWSKI, M., STANKOVIC, D. & FUCHS, L. 2008 Mixing in circular and non-circular jets in crossflow. *Flow Turbul. Combust.* **80**, 255–283.

SANKARAN, R., HAWKES, E. R., CHEN, J. H., LU, T. & LAW, C. K. 2007 Structure of a spatially developing turbulent lean methane–air Bunsen flame. In *31st International Symposium on Combustion*, pp. 1291–1298. The Combustion Institute.

SANKARAN, R., IM, H. G., HAWKES, E. R. & CHEN, J. H. 2005 The effects of non-uniform temperature distribution on the ignition of a lean homogeneous hydrogen–air mixture. In *30th International Symposium on Combustion*, pp. 875–882. The Combustion Institute.

SCHMITT, D. A. 1985 Radiation from a hydrogen flare in crosswind. In *Proceedings of the 23rd AIAA Meeting*, pp. AIAA–1985–0153. American Institute of Aeronautics and Astronautics.

SI, H. 2011 *TetGen: A Quality Tetrahedral Mesh Generator and a 3D Delaunay Triangulator*, first edition. Weierstrass Institute for Applied Analysis and Stochastics (WIAS).

SIMENS, M. P., JIMÉNEZ, J., HOYAS, S. & MIZUNO, Y. 2009 A high-resolution code for turbulent boundary layers. *J. Comput. Phys.* **228**, 4218–4231.

SMITH, S. H. & MUNGAL, M. G. 1998 Mixing, structure and scaling of the jet in crossflow. *J. Fluid Mech.* **357**, 83–122.

SPALART, P. R. 1988 Direct simulation of a turbulent boundary layer up to $R_\theta = 1410$. *J. Fluid Mech.* **187**, 61–98.

SU, L. K. & MUNGAL, M. G. 2004 Simultaneous measurements of scalar and velocity field evolution in turbulent crossflowing jets. *J. Fluid Mech.* **513**, 1–45.

SUTHERLAND, J. C. & KENNEDY, C. A. 2003 Improved boundary conditions for viscous, reactive, compressible flows. *J. Comput. Phys.* **191**, 502–524.

SWAMINATHAN, N. & BILGER, R. W. 1997 Direct numerical simulation of turbulent nonpremixed hydrocarbon reaction zones using a two-step reduced mechanism. *Combust. Sci. Technol.* **127**, 167–196.

SWAMINATHAN, N. & GROUT, R. W. 2006 Interaction of turbulence and scalar fields in premixed flames. *Phys. Fluids* **18** (4).

TAUBIN, G. 1995 A signal processing approach to fair surface design. In *SIGGRAPH*, pp. 351–358.

TOMKINS, C. D. & ADRIAN, R. J. 2003 Spanwise structure and scale growth in turbulent boundary layers. *J. Fluid Mech.* **490**, 37–74.

VEYNANTE, D. & VERVISCH, L. 2002 Turbulent combustion modeling. *Prog. Energy Combust. Sci.* **28**, 193–266.

WU, X. & MOIN, P. 2009 Direct numerical simulation of turbulence in a nominally zero-pressure-gradient flat-plate boundary layer. *J. Fluid Mech.* **630**, 5–41.

YOO, C. S., SANKARAN, R. & CHEN, J. H. 2009 Three-dimensional direct numerical simulation of a turbulent lifted hydrogen jet flame in heated coflow: flame stabilization and structure. *J. Fluid Mech.* **640**, 453–481.